Archives of Civil and Mechanical Engineering (2022) 22:86
https://doi.org/10.1007/s43452-022-00405-9

ORIGINAL ARTICLE

Shape and packing effects in particulate composites: micromechanical modelling and numerical verification

M. Majewski[1] · M. Wichrowski[1,2] · P. Hołobut[1] · K. Kowalczyk-Gajewska[1]

Received: 14 November 2021 / Revised: 8 February 2022 / Accepted: 13 February 2022

Abstract
The aim of this study is to analyse the joint effect of reinforcement shape and packing on the effective behaviour of particulate composites. The proposed semi-analytical modelling method combines the Replacement Mori–Tanaka scheme, by means of which the concentration tensors for non-ellipsoidal inhomogeneities are found numerically, and the analytical morphologically representative pattern approach to account for particle packing. Five shapes of inhomogeneities are selected for the analysis: a sphere, a prolate ellipsoid, a sphere with cavities, an oblate spheroid with a cavity as well as an inhomogeneity created by three prolate spheroids crossing at right angles. Semi-analytical estimates are compared with the results of numerical simulations performed using the finite element method and with the outcomes of classical mean-field models based on the Eshelby solution, e.g. the Mori–Tanaka model or the self-consistent scheme.

Keywords Composite material · Micromechanics · Computational modelling · Packing effect · Shape effect

1 Introduction

For years, new materials had been developed using the empirical approach [1]. Recently, however, this approach has been challenged by micromechanical modelling and simulation strategies [2], which aim to reduce the development time and cost of novel composite materials. A composite material is a combination of two or more constituent materials having markedly different chemical or physical properties. The combined matrix and reinforcement materials can produce a particulate composite of unique characteristics different from those of the constituent elements [3]. These materials may reveal remarkable structural and mechanical properties such as improved resistance to wear, chemicals or fire, and high strength to weight ratio [4]. Their heterogeneous microstructure can be very complex: the filler material may have the form of fragments, particles, or fibres of a natural or synthetic material; the matrix is generally seen as a relatively soft phase with specific properties such as formability, high/low thermal conductivity, and ductility; the bonding between phases affects the macroscopic material behaviour [4]. Understanding of the relationship between morphological features of the microstructure and overall macroscopic properties of heterogeneous materials is essential from the point of view of reliable micromechanical modelling [2].

The classical mean-field micromechanical models (e.g. the standard Mori–Tanaka (MT) or self-consistent (SC) model) are not able to describe the impact of the details of the distribution of components in the representative volume element on the overall properties. As a result, the quality of predictions obtained with such models decreases with an increasing volume fraction of phases and growing contrast in phase properties [5]. Moreover, since those models are based on Eshelby's solution [6], only ellipsoidal shapes of heterogeneities are usually accounted for. To overcome these shortcomings of the available mean-field approaches, some extensions of the existing formulations were proposed for elastic composites. As concerns the effect of particle distribution, among analytical models one can distinguish: (i) variational bounds with n-point correlation functions of elastic moduli [7], e.g. of cracked media [8], or as an application to isotropic dispersions [9]; (ii) the morphologically representative pattern (MRP) approach, e.g. in linear elasticity

✉ M. Majewski
mmajew@ippt.pan.pl

[1] Institute of Fundamental Technological Research, Polish Academy of Sciences, Pawińskiego 5B, 02-106 Warsaw, Poland

[2] Interdisciplinary Center for Scientific Computing, Heidelberg University, Im Neuenheimer Feld 205, 69120 Heidelberg, Germany

Published online: 05 March 2022

with the size effect [10], in comparison with numerical homogenization [11], in linear viscoelasticity [12], in the non-linear elastic–plastic response [13]; (iii) *n*-site versions of mean-field [14], or far-field theories c.f. [15], e.g. cluster models in elastic–viscoplastic composites [16]. A more detailed review of these approaches was presented in [11]. An MRP strategy for describing packing is pursued in the present paper.

In the literature, there are also full-field numerical analyses of representative volume elements of heterogeneous materials by means of the finite element method, e.g. studies of particle spatial distribution [17], particle clustering in the plastic deformation [18], or fast Fourier transform method [19]. The influence of particle shapes on damage properties of composites has been studied in this fashion in [20]. Compared to analytical models, such studies are much more time-consuming, in particular, when a detailed representation of the microstructure is required. Most of the full-field analyses have indicated that packing of particles has a negligible influence on the effective elastic or elastic–plastic response; however, it becomes vital when damage initiation and evolution are involved [18].

To correctly estimate the shape effect on the overall response of heterogeneous materials by means of an analytical model, first it is necessary to accurately describe the effect of a single inhomogeneity on the macroscopic properties of the composite. The shapes of inclusions used in composite materials have a wide spectrum: from the geometrically simplest spheres, through fibres, to the form of complex skeletons. It has been shown in the literature [21] that the uniformity of strain and stress fields proved by Eshelby [6] does not hold for non-elliptic inclusions. Three strategies have been identified in the literature [22] for estimating the composite response in the presence of non-elliptical heterogeneities. The first strategy is to employ analytical procedures for estimating position-dependent Eshelby tensors. In this manner, standard mean-field methods, and especially two approaches: the so-called effective self-consistent scheme [23] and its simplified version—the interaction direct derivative estimate [24], are used in combination with analytical expressions for the Eshelby tensor based on its irreducible decomposition. The effective self-consistent scheme is based on Christensen's work [5], namely on the generalized self-consistent method and its further modification to a three-phase model. The second approach is the Mori–Tanaka method used in combination with the replacement tensor, called the replacement Mori–Tanaka method (RMTM). It uses numerical models of one isolated inhomogeneity embedded in a large region of the matrix material. This procedure was used by Nogales and Böhm [25] in combination with the Mori–Tanaka model to predict the thermal conductivity of diamond-reinforced composites. The technique is an alternative approach to the compliance contribution formalism of Kachanov et al. [26]. The final strategy is to directly discretize the microstructure's domain using, e.g. the finite element method (FEM). Usually, the computation of the macroscopic behaviour is performed for a representative volume element (RVE) which is defined as the smallest region of the composite that accurately describes the material response. The calculation of the minimum RVE size is a non-trivial task (e.g. [27]). In several papers, estimations of effective properties obtained using RVEs for periodic (e.g. [28]) and non-periodic structures (e.g. [29]) have been presented.

The focus of the present study is on the extension of the MRP approach to account for the combined effect of particles' shape and packing. The standard MRP approach was extensively verified for elastic [11] and elastic–plastic [13] composites with spherical inhomogeneities, where MRP results were confronted with outcomes of computational homogenization by FEM. The present research is a continuation of these studies and addresses the issue of applicability of the MRP approach to describing the effect of the inhomogeneities' shape on the response of particulate composites. It is shown that an important modification of the standard formulation of the MRP scheme is required to this end. The calculated estimations are evaluated through comparison with the results of corresponding FE simulations. The FE analyses are performed using periodic unit cells with face-centred cubic (FCC) arrangements of particles and RVE with randomly placed inhomogeneities. In the latter case, the applied algorithm for generating RVEs is an extended version of the procedure presented in [11].

The paper is constructed as follows. In the next section, we briefly outline the theoretical foundations of the developed MRP mean-field model: first, we provide a description of the proposed micromechanical mean-field approach, then we introduce inclusions of complex shape to the model. In Sect. 3, we discuss the numerical finite element method applied to this problem and the procedures used for generating periodic unit cells and RVEs involving random particle distributions with varying inclusion shapes and values of the packing ratio. In Sect. 4, we present a comparison of the results obtained using the mean field and the FE methods for two-phase composites in the case of both unit cells and RVEs. Finally, in the last section, we summarize the main results presented in this paper.

2 Micromechanical MRP model

2.1 Morphologically representative pattern approach

The morphologically representative pattern approach [13] studied in this paper originates from the composite sphere

model formulated in [30] for a two-phase material, and its further modification to the generalized self-consistent (GSC) scheme in [5]. Within the GSC model, also referred to as a three-phase model, a single composite sphere is considered which, similarly to the inhomogeneity in the self-consistent model, is embedded in an equivalent homogeneous medium with effective properties. In the succeeding years, the GSC 3-phase configuration was extended to the n-phase version by Herve and Zaoui [31], who solved the problem of the composite sphere with n coatings and formulated the n-phase generalized self-consistent (n-GSC) scheme. In [11], the n-GSC and SC schemes were combined with the MRP model in the case of spherical inhomogeneities. The present study focuses on the effect of particle shape on the overall material response, and this will be analyzed using the RMTM. Thus, the MRP approach is reformulated here by employing the Mori–Tanaka-like model, instead of the GSC scheme as in [11]. The MRP model reformulated in this way is significantly different from the MRP approach presented in the previously mentioned papers [10–13].

The MRP approach postulates a subdivision of the RVE with some morphological features into M representative patterns α with specified volume contributions c_α to the overall RVE volume V. Within each pattern α, the volume fraction of phase k is assumed to be f_k^α, with f_k being the volume fraction of phase k in the entire RVE, so that

$$\begin{aligned} &c_\alpha = \frac{V_\alpha}{V}\,, \quad \sum_{\alpha=1}^{M} c_\alpha = 1\,, \quad f_k^\alpha = \frac{V_\alpha^k}{V_\alpha}\,, \\ &\sum_{\alpha=1}^{M} c_\alpha f_k^\alpha = \frac{V_k}{V} = f_k\,, \quad \sum_{k=1}^{N} f_k = 1\,, \end{aligned} \tag{1}$$

where V_α is the volume of pattern α, V_α^k is the volume of phase k in pattern α, and N is the number of phases in the composite. Let us emphasize that c refers to the volume fraction of patterns in the composite material's volume and f to the volume fraction of composite phases or their portions. We used the two different symbols, c and f, to emphasize the difference between the two mentioned quantities.

In the case of a linear problem (i.e. elasticity, viscosity), the average strain $\boldsymbol{\varepsilon}_k^\alpha$ in the phase k of pattern α is approximated by using the auxiliary far-field strain $\mathbf{E}_0$ and a fourth-order concentration tensor $\mathbb{A}_k^\alpha$, namely

$$\boldsymbol{\varepsilon}_k^\alpha = \mathbb{A}_k^\alpha \cdot \mathbf{E}_0\,. \tag{2}$$

The far-field strain $\mathbf{E}_0$ is the same for all patterns and in general is not equal to the overall average strain $\mathbf{E}$ in the RVE. The relation between the two quantities is as follows:

$$\mathbf{E} = \langle \boldsymbol{\varepsilon} \rangle_V = \sum_{\alpha=1}^{M} c_\alpha \sum_{k=1}^{N} f_k^\alpha \boldsymbol{\varepsilon}_k^\alpha = \sum_{\alpha=1}^{M} c_\alpha \sum_{k=1}^{N} f_k^\alpha \mathbb{A}_k^\alpha \cdot \mathbf{E}_0\,, \tag{3}$$

where $\boldsymbol{\varepsilon}$ is the strain field in the representative volume V and $\langle \cdot \rangle_V$ is the volume averaging operation defined as $1/V \int_V (\cdot) dV$. Using the above condition, the average strain $\boldsymbol{\varepsilon}_k^\alpha$ is specified by the strain concentration relation of the form

$$\begin{aligned} \boldsymbol{\varepsilon}_k^\alpha &= \mathbb{A}_k^\alpha \left(\sum_{\beta=1}^{M} c_\beta \sum_{j=1}^{N} f_j^\beta \mathbb{A}_j^\beta \right)^{-1} \cdot \mathbf{E} = \overline{\mathbb{A}}_k^\alpha \cdot \mathbf{E}\,, \\ &\text{where} \quad \sum_{\alpha=1}^{M} c_\alpha \sum_{k=1}^{N} f_k^\alpha \overline{\mathbb{A}}_k^\alpha = \mathbb{I}\,. \end{aligned} \tag{4}$$

Utilizing the constitutive law $\boldsymbol{\sigma}_k^\alpha = \mathbb{L}_k^\alpha \cdot \boldsymbol{\varepsilon}_k^\alpha$ and the expression for the overall average stress $\boldsymbol{\Sigma} = \langle \boldsymbol{\sigma} \rangle_V$, the overall constitutive law is obtained:

$$\boldsymbol{\Sigma} = \left(\sum_{\alpha=1}^{M} c_\alpha \sum_{k=1}^{N} f_k^\alpha \mathbb{L}_k^\alpha \overline{\mathbb{A}}_k^\alpha \right) \cdot \mathbf{E} = \overline{\mathbb{L}} \cdot \mathbf{E}\,, \tag{5}$$

in which the fourth-order tensor $\overline{\mathbb{L}}$ is the effective material stiffness. In this analysis, the basic configuration of the MRP approach is verified for two-phase isotropic particulate composites (Table 1) against the outcomes of numerical homogenization. This simplest case, in which the microstructure is represented by only two patterns ($M = 2$, see Fig. 1), allows us to explore packing and shape effects, namely:

- To account for the shape effect, the first pattern is treated with the replacement Mori–Tanaka model, i.e. the concentration tensor of the inclusion is calculated via the fast numerical method described in the next section (Sec.2.2), combined with the double-inclusion framework of [32].
- To account for the packing effect, in the RMTM pattern, the volume fraction of the matrix coating f_λ is specified by the minimum distance between nearest-neighbour particles ($2\lambda_k$ in Fig. 1). In other words, λ_k is half of the distance between inclusion k and its nearest neighbour (if they are in contact, $\lambda_k = 0$). $f_{\lambda k}$ is the volume fraction of the matrix material lying within a distance λ_k of inclusion k, so $f_{\lambda k}$ depends on the distance between particles, i.e. their packing. For example, in the case of spherical particles and assuming a unit material volume, we have $f_{\lambda k} = 4/3\,\pi\left(\left(R_k + \lambda_k\right)^3 - \left(R_k\right)^3 \right)$, where R_k is the radius of inclusion k. f_λ is the volume fraction of all inclusion coatings $f_{\lambda k}$ in the RVE, which is $f_\lambda = \Sigma_{k=1}^{N_i} f_{\lambda k}$ and N_i is the number of inclusions. Thus, when all inclusions are in contact, all λ_k are 0 and so $f_\lambda = 0$ in the RMTM pattern.

At variance with the previous analyses [11], to additionally take into account the influence of the inclusion on the surrounding matrix beyond the f_λ region, a second

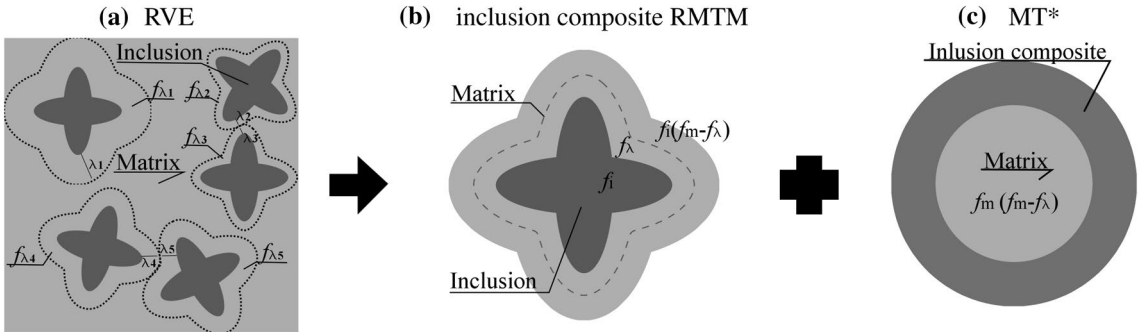

Fig. 1 The microstructure of a two-phase composite reinforced with non-ellipsoidal inclusions $k = 1, \ldots, 5$ of the same size and shape, represented in the MRP approach by two patterns: RMTM and MT*. Above, λ_k equals half the distance between inclusion k and its nearest neighbour, $f_{\lambda k}$ is the volume fraction of the matrix material lying within a distance λ_k of inclusion k, f_λ is the volume fraction of all inclusion coatings $f_{\lambda k}$ in the RVE, which is $f_\lambda = \Sigma_{k=1}^{5} f_{\lambda k}$ in the presented example, f_i is the volume fraction of all inclusions, and $f_m = 1 - f_i$ is the volume fraction of the matrix

Table 1 Assumed material parameters of the metal matrix composite (MMC) reinforced with ceramic particles [33]

Phase	Ceramic	Metal
Young's modulus, E [GPa]	400	75
Poisson's ratio, ν	0.2	0.3

coating with a volume fraction $f_i(f_m - f_\lambda)$ is added to the RMTM pattern. The second pattern (denoted by MT*) is a Mori–Tanaka-type problem applied to the remaining matrix material $f_m(f_m - f_\lambda)$ (see Fig. 1). In other words, in the simplest case of a two-pattern system four domains are distinguished:

- in the RMTM pattern: inclusions f_i; the first matrix coating f_λ, which describes the packing of inclusions; the second matrix coating $f_i(f_m - f_\lambda)$, which represents the inclusions' influence on the matrix outside the λ domain;
- and in the MT-like pattern: the rest of the matrix $f_m(f_m - f_\lambda)$, which is treated as a spherical inhomogeneity surrounded by a medium having the composite inclusion (RMTM) properties. Since the roles played by the matrix and inclusion phases are inverted by such treatment, we refer to this pattern shortly as the inverse MT and denote it by MT*.

In such a two-pattern system, the volume fractions of the patterns of the RMTM and MT* type, respectively, are

$$c_{RMTM} = f_i + f_\lambda + f_i(f_m - f_\lambda), \quad c_{MT} = 1 - c_{RMTM}, \tag{6}$$

where f_i is the volume fraction of inclusions in the composite, and $f_m = 1 - f_i$ is the volume fraction of the matrix in a two-phase composite.

For the basic two-pattern MRP approach as in Fig. 1, the effective stiffness $\overline{\mathbb{L}}$ of the composite (Eq. 5) is specified as

$$\begin{aligned}\overline{\mathbb{L}} = {} & f_i \mathbb{L}_i \overline{\mathbb{A}}_i^{RMTM} + f_\lambda \mathbb{L}_m \overline{\mathbb{A}}_m^{RMTM,1stcoat} \\ & + f_i(f_m - f_\lambda)\mathbb{L}_m \overline{\mathbb{A}}_m^{RMTM,2ndcoat} \\ & + f_m(f_m - f_\lambda)\mathbb{L}_m \overline{\mathbb{A}}_m^{MT*}.\end{aligned} \tag{7}$$

The range of the second coating specified by $f_i(f_m - f_\lambda)$ in the RMTM pattern resulted from multiple trials and comparison with numerical data, and it provides the best predictions for the considered non-spherical shapes. We remark that, in the present context of the RMTM treatment of the composite inclusion in the first pattern and linear elastic properties, the approach is equivalent to taking a single coating with a volume fraction $f_\lambda + f_m(f_m - f_\lambda)$. This will change if elastic–plastic response is analysed and the n-GSC pattern is used instead. The remaining matrix $f_m(f_m - f_\lambda)$ in the MT* pattern is assumed as spherical because the matrix is surrounded by the composite inclusions in an isotropic manner.

For a fixed f_i, the MRP model predictions depend on the volume fraction f_λ, determined by the minimum distance between nearest-neighbour particles λ, and the total volume fraction of the matrix $f_m = 1 - f_i$. The smallest distance λ between the surfaces of inclusions was computed numerically. Let us define the matrix packing ratio f_λ / f_m. Two limit cases for the ratio f_λ / f_m equal to 1 and 0, respectively, can be considered. In the first limit, all matrix material is used to form the coating of the inclusion in the RMTM pattern, $f_\lambda = f_m$, thus the packing ratio is 1. In the second one, each particle k touches its nearest neighbour, so $\lambda_k = 0$, and thus $f_\lambda = 0$ and the packing ratio is 0. In the first case, the volume fraction of the MT* pattern is zero, so the MRP solution reduces to the RMTM estimate. In the second case, the

influence of the RMTM pattern is reduced to the inclusion f_i and the second coating $f_i \cdot f_m$, and the MRP estimate lies between the standard MT and reverse MT solutions. The reverse MT solution is obtained by considering a composite of the same microstructure geometry as the original one, but for which the matrix and inclusion materials are reversed. Without the second coating $f_i(f_m - f_\lambda)$ in the RMTM pattern, for $f_\lambda = 0$ the MRP equals the reverse MT.

This article presents numerical results for two sets of tests. In the first set, a metal-matrix composite (MMC) reinforced with ceramic inclusions of various volume fractions and particle arrangements is studied, with phase properties kept constant. In the second set, the material parameters of the two-phase composite are varied to demonstrate the effect of phase contrast on the agreement between predictions of the proposed variant of the MRP model and the results of FE simulations.

To illustrate the impact of the matrix packing ratio in the proposed variant of the MRP model on the effective properties of composites, results for the MMC composite with spherical inclusions are presented first in this section.

Figure 2 shows the variation of MRP estimates induced by changing the matrix packing ratio f_λ/f_m, using the example of the effective shear modulus $\overline{G}$. The value is scaled by the shear modulus of the softer phase G_s. The material parameters are listed in Table 1. We study two configurations of the particulate composite: (I) with a soft matrix reinforced with a hard (stiffer) phase $f_i = f_h$ (marked by black dots), or (II) with the matrix stiffer than inclusions, where $f_m = f_h$ (marked by circles). Fig. 2a presents the effective shear modulus $\overline{G}$ as a function of the matrix packing ratio f_λ/f_m. The classical micromechanical models: Mori–Tanaka, mean MT calculated as the average $\overline{\mathbb{L}}$ of two composite configurations (i.e. with hard or soft particles, respectively), self-consistent scheme and its extension to the three-phase generalized self-consistent scheme (3-GSC) do not depend on the packing ratio, so they are represented by horizontal lines in Fig. 2a. Moreover, mean MT and SC estimates do not distinguish between the composite configurations with hard vs soft inhomogeneities. Among the presented estimates, only the MRP approach takes into account the influence of the packing ratio f_λ/f_m. The previous formulation of the MRP model from [11] based on the 3-GSC and SC schemes for two patterns, denoted by grey curves (Fig. 2a), starts from the SC solution for $f_\lambda/f_m = 0$ and approaches the 3-GSC one for $f_\lambda/f_m = 1$. The present modified MRP model, based on the RMTM (equivalent to MT for spheres) and MT*

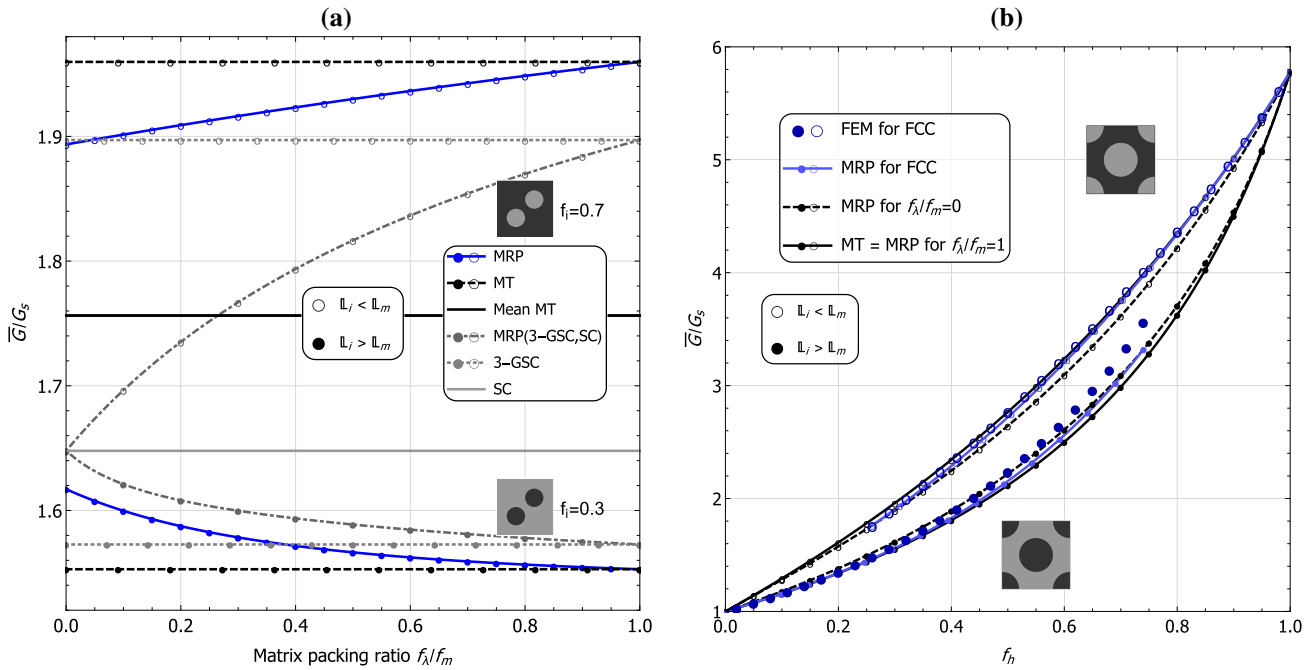

Fig. 2 The effective shear modulus $\overline{G}$ vs **a** the packing ratio f_λ/f_m, **b** the volume fraction of the hard phase f_h. The value is scaled by the shear modulus of the softer phase G_s. Notation: *MRP* the present variant of the MRP model based on two MT-type patterns, *MT* the Mori–Tanaka method, *Mean MT* the average $\overline{\mathbb{L}}$ of two configurations (hard or soft particles) by the MT model, *MRP(3-GSC,SC)* the previous variant of the MRP model [11] based on the 3-GSC and SC schemes, *3-GSC* the 3-phase generalized self-consistent scheme, *SC* the self-consistent scheme, *FEM* numerical homogenization. A two-phase composite as in Table 1 with a continuous matrix and spherical particles. In **b**, the packing ratio varies with the volume fraction as for the particles in the face-centred cubic arrangement [in FEM results, $\overline{G}$ is calculated for the shear deformation specified by $\mathbf{E}^{(2)}$ in Eq. (19)]

schemes, denoted by blue lines (Fig. 2a), approaches the MT estimate for $f_\lambda/f_m = 1$ and displays a smaller packing effect compared to the previous version towards $f_\lambda/f_m = 0$ for the hard inclusions case.

Let us now consider the spherical particle arrangements as in the periodic face-centred cubic lattice (Fig. 9a). In this case, when the positions of particles are fixed, the matrix packing ratio f_λ/f_m depends on the inclusion volume fraction f_i and attains its limit $f_\lambda/f_m = 0$ for $f_i \approx 0.74$. Fig. 2b shows the effective shear modulus $\overline{G}$ as a function of the volume fraction of the hard phase f_h. As f_i tends to 0.74 (for hard inclusions $f_h \to 0.74$, and for a hard matrix $f_h \to 0.26$), the MRP results and the MT scheme predictions diverge. Thus, similarly to the former variant of the MRP model, for the hard (respectively soft) inclusion case, an additional increase (respectively decrease) in stiffness is observed when the packing ratio increases, compared to the standard MT model. However, this stiffening (or softening, respectively) is smaller compared to the previous MRP variant. For the sake of validation, corresponding results obtained using numerical homogenization (FEM) are also presented. It is worth emphasizing that the reliability of the FEM simulation depends on the quality of the mesh. As discussed in [11], the effective stiffness obtained numerically for an FCC-type unit cell has cubic symmetry, therefore, in general, two different shear moduli are found depending of the loading conditions. The presented value of $\overline{G}$ corresponds to the shear deformation of the form given by $\mathbf{E}^{(2)}$ in Eq. (19). Nevertheless, it was found in [11] that for the FCC unit cell a similar variation of results is obtained for the second shear modulus—the one corresponding to the shear deformation given by $\mathbf{E}^{(1)}$ in Eq. (19).

2.2 Accounting for the shape of inhomogeneities in the RMTM method

In [22], a method of finding concentration tensors for inhomogeneities of a non-spherical shape was proposed within the context of the Mori–Tanaka averaging scheme. We briefly recall the resulting scheme referred to as the replacement Mori–Tanaka method. The described procedure is next used to find $\mathbb{A}_i^{RMTM}$ required for the present variant of the MRP approach when the shape of the inhomogeneity is not ellipsoidal.

The Mori–Tanaka method [34] approximates the response of an inhomogeneous material for a non-diluted volume fraction of inhomogeneities via diluted ones that are loaded by the effective or averaged matrix stress or strain, respectively. Mori and Tanaka [34] assumed that each inhomogeneity is placed in a boundless matrix and remotely subjected to the average matrix stress $\boldsymbol{\sigma}_m$ or strain $\boldsymbol{\varepsilon}_m$. Hence, the central assumption of the MT method for elasticity can be formulated as

$$\boldsymbol{\varepsilon}_i = \mathbb{A}_i^{Dil}\boldsymbol{\varepsilon}_m = \mathbb{A}_i^{Dil}\mathbb{A}_m^{MT}\mathbf{E} = \mathbb{A}_i^{MT}\mathbf{E}, \tag{8}$$

where $\boldsymbol{\varepsilon}_i$ and $\boldsymbol{\varepsilon}_m$ are the averaged inhomogeneity and matrix strain, respectively, $\mathbb{A}_m^{MT}$ is the matrix Mori–Tanaka strain concentration tensor, $\mathbf{E}$ is the macroscopic strain, and $\mathbb{A}_i^{Dil}$ is the diluted strain concentration tensor. In the case of an ellipsoidal inhomogeneity, it is specified as

$$\mathbb{A}_i^{Dil} = \left[\mathbb{I} + \mathbb{P}_m\left(\mathbb{L}_i - \mathbb{L}_m\right)\right]^{-1}, \tag{9}$$

where $\mathbb{P}_m$ is the polarization tensor, which is known for ellipsoidal shapes [6] and depends on the matrix stiffness $\mathbb{L}_m$, $\mathbb{I}$ is the fourth-rank identity tensor, while $\mathbb{L}_i$ and $\mathbb{L}_m$ are the elasticity tensors of the inhomogeneity and the matrix phase, respectively. Following the standard procedure of the mean-field approach, one can obtain the effective material stiffness $\overline{\mathbb{L}}_{MT}$ as

$$\overline{\mathbb{L}}_{MT} = \mathbb{L}_m + f_i\left(\mathbb{L}_i - \mathbb{L}_m\right)\mathbb{A}_i^{MT}, \tag{10}$$

in which f_i is the volume fraction of the inhomogeneity phase in the composite, and $\mathbb{A}_i^{MT}$ is the inhomogeneity Mori–Tanaka strain concentration tensor specified as

$$\mathbb{A}_i^{MT} = \left[f_i\,\mathbb{I} + f_m\left(\mathbb{A}_i^{Dil}\right)^{-1}\right]^{-1}. \tag{11}$$

Thus for a two-phase material, the Mori–Tanaka method takes into account interaction between the phases. Remark that the application of the MT to multi-phase composites is sometimes questionable (e.g. [7]). The main obstacle is that the major (diagonal) symmetry of the estimated stiffness tensor is violated. However, this is not an issue in the present analysis since we study a two-phase composite, namely a metal matrix reinforced with ceramic particles (Table 1).

In the case of non-ellipsoidal inclusions, the analytical form of the diluted strain concentration tensor of the inhomogeneity $\mathbb{A}_i^{Dil}$ (Eq. 9) is not known. Therefore, following [22], a phase-averaged diluted "replacement" is introduced. Firstly, in Eq. 11, the analytical strain concentration tensor $\mathbb{A}_i^{Dil}$ is replaced with its numerical approximation $\mathbb{A}_i^{NDil}$. Consequently, the strain concentration tensor $\mathbb{A}_i^{RMTM}$, replacing $\mathbb{A}_i^{MT}$, is given by

$$\mathbb{A}_i^{RMTM} = \left[f_i\,\mathbb{I} + f_m\left(\mathbb{A}_i^{NDil}\right)^{-1}\right]^{-1}. \tag{12}$$

Secondly, a phase-averaged diluted "replacement" elasticity tensor $\mathbb{L}_i^{NDil}$ is used instead of $\mathbb{L}_i$ in Eq. 10. Therefore, the effective material stiffness $\overline{\mathbb{L}}_{RMTM}$ is

$$\overline{\mathbb{L}}_{RMTM} = \mathbb{L}_m + f_i\left(\mathbb{L}_i^{NDil} - \mathbb{L}_m\right)\mathbb{A}_i^{RMTM}. \tag{13}$$

The phase-averaged diluted "replacement" elasticity tensor $\mathbb{L}_i^{NDil}$ is obtained from the relation of the form

$$\mathbb{L}_i^{NDil} = \mathbb{L}_m + \left(f_i^{NDil}\right)^{-1}\left(\overline{\mathbb{L}}_{NDil} - \mathbb{L}_m\right)\left(\mathbb{A}_i^{NDil}\right)^{-1}, \tag{14}$$

where $\overline{\mathbb{L}}_{NDil}$ and f_i^{NDil} are the effective stiffness tensor and the inhomogeneity volume fraction for the analysed unit cell with a diluted inhomogeneity of an arbitrary shape, respectively. Both $\overline{\mathbb{L}}_{NDil}$ and $\mathbb{A}_i^{NDil}$ are obtained numerically, e.g. using the finite element method. We provide further details of the procedure is explained in the next section (Sec.3).

In the rest of this paper, we restrict ourselves to five shapes of inhomogeneities, namely:

- a sphere (Fig. 3a),
- a prolate spheroid with semi-axes $(2a, a, a)$ (Fig. 3b),
- a sphere with identical cylindrical cavities in three mutually perpendicular directions (drilled sphere); the ratio of the sphere's radius to the diameter of the cylinders is assumed to be constant and equal to $R_{Sph}/d_{Cyl} = 3/2$ (Fig. 3c),
- three prolate spheroids with semi-axes $(2a, a, a)$ crossing at right angles (Fig. 3d),
- an oblate spheroid with semi-axes $(2/3\,a, a, a)$, with a cylindrical cavity in the 'X' principal axis direction (drilled oblate spheroid); the cylinder's diameter is assumed to satisfy $a/d_{Cyl} = 4$ (Fig. 3e).

The first two ellipsoidal shapes are considered mainly for the purpose of comparison, to verify the procedure of computing the $\mathbb{A}_i^{NDil}$ tensor.

In Fig. 3f, planar projections of the five inclusion types with the same volume are compared.

It is worth noting that the matrix packing ratio f_λ/f_m of inclusions with cavities (Fig. 3c and e) is still computed as the ratio of the volume of the matrix coating f_λ around the inclusion, without the matrix in the cavity, to the volume of the entire matrix f_m in the composite. The matrix in the cavity is considered as part of the matrix in the MT* pattern of the "free matrix". With this assumption, if an inclusion with a cavity touches its nearest neighbour, f_λ/f_m equals 0. The matrix coating has the same shape as the inclusion (e.g. Fig. 1b). In the case of drilled inhomogeneities (Fig. 3c and e) the cavities are neglected, e.g. the matrix coating of the drilled sphere (Fig. 3c) is spherical.

3 Numerical procedures

3.1 Numerical concentration tensors

As it was mentioned earlier, $\overline{\mathbb{L}}_{NDil}$ and $\mathbb{A}_i^{NDil}$ are obtained numerically using the FEM. The tetrahedral meshes for the unit cells and RVEs have been generated using NetGen [35] and then used in the AceFEM environment [36] to perform the FE computations. A single inhomogeneity of an appropriate shape and properties is embedded in a large, but finite matrix region (Fig. 4).

The strain concentration tensor $\mathbb{A}_i^{NDil}$ is obtained from volume averages over the inhomogeneity and $\overline{\mathbb{L}}_{NDil}$ through numerical homogenization of the entire sample. In particular, the following relations are used:

$$\boldsymbol{\varepsilon}_i = \mathbb{A}_i^{NDil}\boldsymbol{\varepsilon}_m\,, \quad \boldsymbol{\Sigma} = \overline{\mathbb{L}}_{NDil}\mathbf{E}\,, \tag{15}$$

in which $\mathbf{E}$ is the strain imposed by means of the periodic boundary conditions as described below, $\boldsymbol{\Sigma}$ is the stress averaged over the whole cell, while $\boldsymbol{\varepsilon}_i$ and $\boldsymbol{\varepsilon}_m$ are the strains averaged over the inhomogeneity and matrix, respectively.

For this purpose, 3D numerical models of the matrix-inhomogeneity arrangement with a single diluted inhomogeneity $f_i^{NDil} = 10^{-4}$, as shown in figure Fig. 4, are

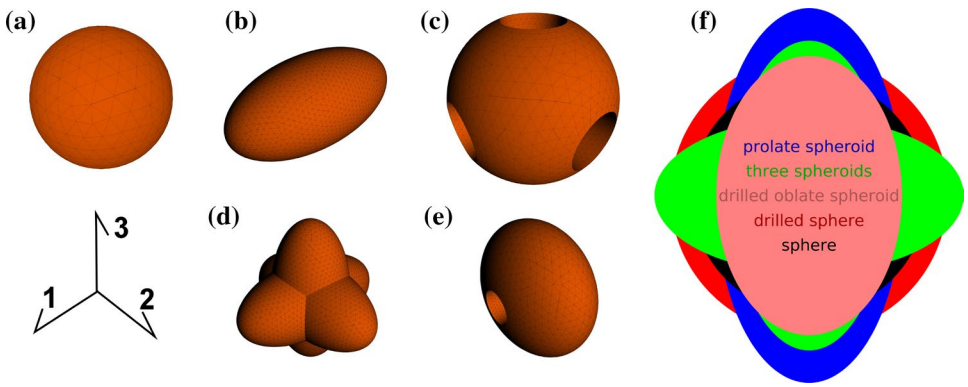

Fig. 3 Five selected inclusion shapes: **a** a sphere, **b** a prolate spheroid with semi-axes $(2a, a, a)$, **c** a drilled sphere, having three identical perpendicular cylinderical cavities with $R_{Sph}/d_{Cyl} = 3/2$, **d** three prolate spheroids with semi-axes $(2a, a, a)$ crossing at right angles, **e** a drilled oblate spheroid with semi-axes $(2/3\,a, a, a)$, having a cylindrical cavity in the 'X' principal direction with $a/d_{Cyl} = 4$. **f** Comparison of the five shapes when they are of the same volume

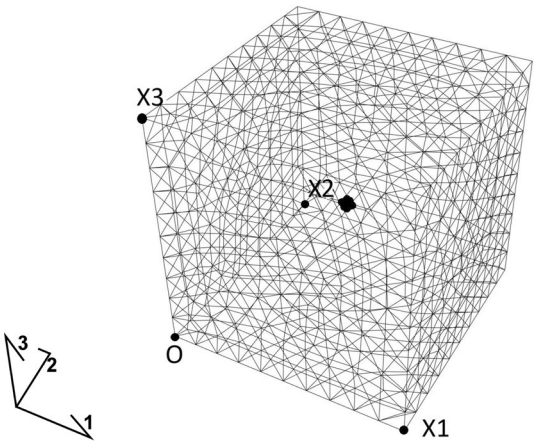

Fig. 4 A single inhomogeneity of an appropriate shape and properties embedded in a large but finite matrix region, used to calculate numerically both the effective stiffness tensor $\underline{\mathbb{L}}_{NDil}$ and the numerical strain concentration tensor $\mathbb{A}_i^{NDil}$

generated and simulated by FEM using a very fine mesh. The mesh size was selected so that a subsequent mesh refinement does not affect the calculated concentration tensors noticeably, i.e. the difference is less than 0.1%. The inhomogeneities and their meshes are shown in Fig. 3a–e. Perfect bonding between phases is used.

We used AceFEM-based in-house code in our calculations. As an alternative, one can use the open-access software AMAT [37], which has similar capabilities. The latter open-access software uses a mesh free method based on a class of Gaussian approximating functions to calculate the components of compliance and stiffness contribution tensors of inhomogeneities of any shape. Both approaches: the one using FEM described in this paper and the AMAT software from the NMSU Center for Micromechanics, give similar results. In this work, we used our FEM codes due to our future plans for code modification to model propagation of cracks. Nonetheless, in the case of calculations involving many different inclusion shapes, e.g. inclusion shape optimization, the AMAT software is more efficient.

We assumed that the effective response of a unit cell is driven solely by the symmetry of the inhomogeneity, possible because we consider a very small volume fraction of inhomogeneity. Consequently, both the fourth-order tensors $\overline{\mathbb{L}}_{NDil}$ and $\mathbb{A}_i^{NDil}$ of the unit cells are:

- isotropic for a spherical inhomogeneity (Fig. 3a),
- of cubic symmetry (Eq. A.6) for the drilled sphere and crossed spheroids (Fig. 3c and d),
- transversely isotropic for the prolate and oblate spheroids (Fig. 3b and e).

Relevant formulae for the projectors stemming from the spectral decomposition of the fourth-order tensors of transverse isotropy and cubic symmetry are given by Eqs. (A.2)–(A.4) and Eqs. (A.7), respectively. They are subsequently used to define independent components of $\overline{\mathbb{L}}_{NDil}$ in 6 and of $\mathbb{A}_i^{NDil}$ in 7.

To derive $\overline{\mathbb{L}}_{NDil}$ or $\mathbb{A}_i^{NDil}$, sets of micro-periodic displacement boundary conditions were imposed on pairs of corresponding points A–B on the opposite faces of a unit cell, viz.

$$\mathbf{u}_A - \mathbf{u}_B = \mathbf{E} \cdot (\mathbf{x}_A - \mathbf{x}_B)\,, \tag{16}$$

where $\mathbf{E}$ is the imposed overall strain of a unit cell equivalent to the local strain averaged over the RVE's volume, $\mathbf{E} = 1/V \int_V \boldsymbol{\varepsilon}\, dV$, while $\mathbf{u}_A$, $\mathbf{u}_B$, $\mathbf{x}_A$ and $\mathbf{x}_B$ are the displacements and initial positions of points A and B, respectively. In the calculations, unit dimensions of the unit cell or RVE were assumed. To realize boundary conditions (Eq.16) in FE analysis, a special multi-point constraint procedure was used. Within this procedure, displacements of a pair of nodes A and B are related to the displacements of two nodes O and Xk at the selected unit cell corners as follows:

$$\mathbf{u}_A - \mathbf{u}_B = \mathbf{u}_O - \mathbf{u}_{Xk}\,, \quad k = 1 \text{ or } 2 \text{ or } 3\,, \tag{17}$$

where $\mathbf{x}_B - \mathbf{x}_A = \mathbf{x}_{Xk}$, and $x_i^{(X1)} = (1,0,0)$, $x_i^{(X2)} = (0,1,0)$, $x_i^{(X3)} = (0,0,1)$, $x_i^{(O)} = (0,0,0)$. For example, index $k = 1$ is taken for the face nodes A and B with coordinates $(0, x_2, x_3)$ and $(1, x_2, x_3)$, respectively. Components of the overall strain $\mathbf{E}$ are then imposed simply by assigning displacement components to the nodes Xk in such a way that

$$u_i^{(Xk)} = (E_{1k}, E_{2k}, E_{3k}). \tag{18}$$

Node O is fixed: $u_i^{(O)} = (0,0,0)$. All coordinates are given in the frame aligned with the main symmetry axes of the cell (see e.g. Fig. 4).

The imposed overall strains are selected based on the eigensubspaces of the effective stiffness tensor. Their representations in the basis $\{\mathbf{m}_i\}$ aligned with the main symmetry axes of the cell are:

$$\begin{aligned} E_{ij}^{(0)} &= \begin{pmatrix} d & 0 & 0 \\ 0 & d & 0 \\ 0 & 0 & d \end{pmatrix}, \quad E_{ij}^{(1)} = \begin{pmatrix} d & 0 & 0 \\ 0 & -d/2 & 0 \\ 0 & 0 & -d/2 \end{pmatrix}, \\ E_{ij}^{(2)} &= \begin{pmatrix} 0 & 0 & 0 \\ 0 & 0 & d \\ 0 & d & 0 \end{pmatrix}, \quad E_{ij}^{(3)} = \begin{pmatrix} 0 & d & 0 \\ d & 0 & 0 \\ 0 & 0 & 0 \end{pmatrix}, \end{aligned} \tag{19}$$

where d specifies the strain magnitude. For transverse isotropy, analysis is performed for all strain forms $\mathbf{E}^{(0)}$ to $\mathbf{E}^{(3)}$, whereas for cubic anisotropy only for $\mathbf{E}^{(0)}$ to $\mathbf{E}^{(2)}$, from the set given in Eq. (19).

In numerical homogenization, five (respectively, three) independent components of $\overline{\mathbb{L}}_{NDil}$ are computed using

Eq. A.5 (respectively, Eq. A.8) for the transverse isotropy case (respectively, cubic symmetry). Similarly, the components of $\mathbb{A}_i^{NDil}$ are derived from Eq. B.3 for the prolate and oblate spheroids, and from Eq. B.3b for other shapes. In general, when the inclusion has an irregular shape, its concentration tensor is usually anisotropic. The numerical simulations should be carried out in such a way as to identify all independent components of the concentration tensor [38].

3.2 Generation of periodic cubes with randomly placed inclusions

Model-based assessments of the influence of the shape and packing of inhomogeneities on the macroscopic behaviour of particulate composites were verified by performing numerical homogenization. Samples with both regular and random arrangements of particles were generated. The results for composites with inclusions placed as in the FCC system (Fig. 9) are presented in Subsect. 4.2, while those with random arrangements of inclusions (e.g. Figs. 5 or 6) are described in Subsect. 4.3.

The cubic volume elements with randomly placed particles were generated using a discrete element method (DEM)-based dynamic procedure. This particular method was chosen due to its availability via existing DEM software, its ability to handle volume fractions reaching 0.65, and its speed of execution. The application of technique itself, when applied to spherical inclusions, was described in the previous paper [11]. Here we only note that inclusions, represented by elastic spheres, are initially placed in an enlarged periodic cell, which subsequently shrinks to its target dimensions $1 \times 1 \times 1$. During the compression, the spheres mix and collide, which results in their desired pseudo-random placement in the final cell (e.g. Fig. 5). For the purposes of this paper we used the Yade DEM software [39].

In the case of microstructures with spheroidal inclusions (Fig. 6b–d), first the positions of inclusions' centres were randomly selected using the above algorithm, and then random directions of each inclusion's main axes of

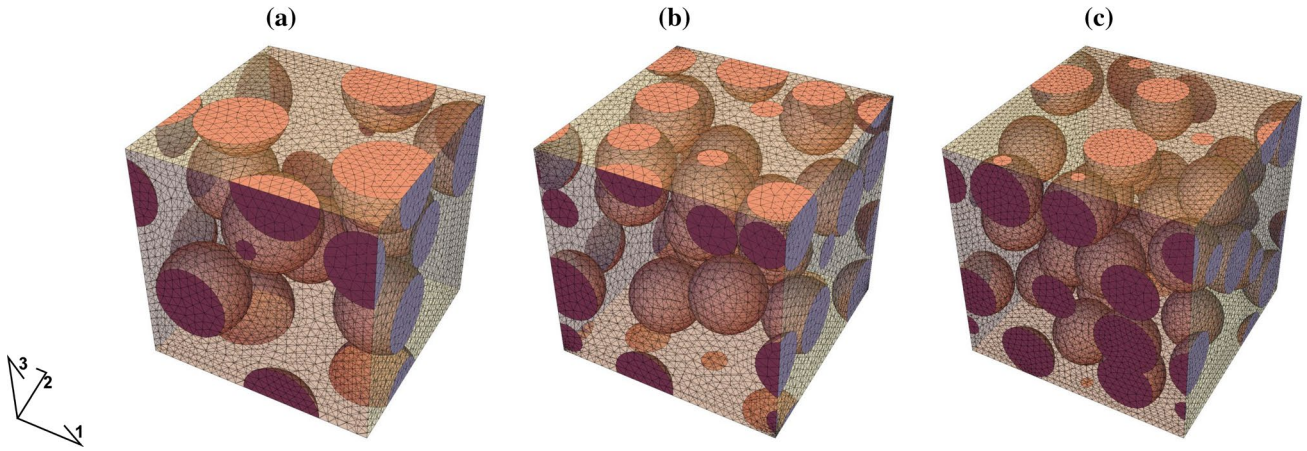

Fig. 5 Volume elements with periodic boundaries and **a** 10, **b** 20, and **c** 30 randomly placed spheres. The volume fraction of inclusions is 30%

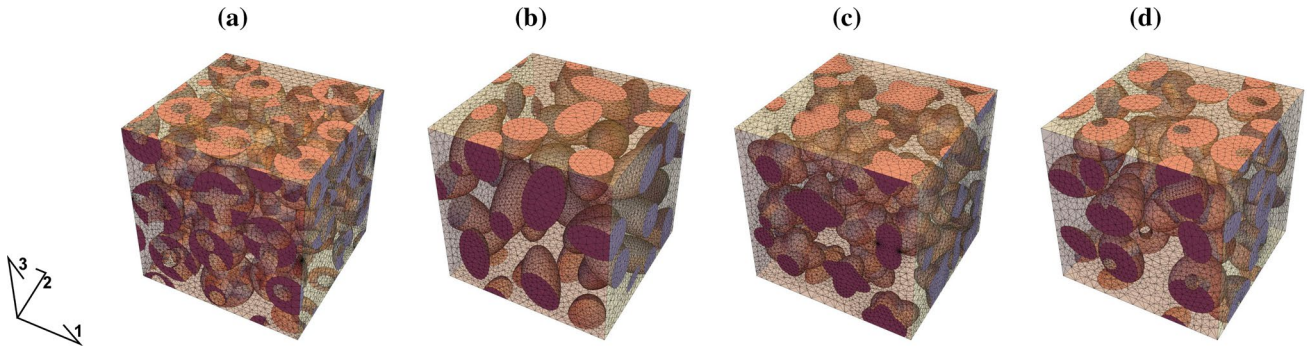

Fig. 6 Representative volume elements with periodic boundaries, randomly generated structures, and the volume fraction of 30 inclusions equal to 30%. The shapes of inclusions are: **a** drilled spheres (Fig. 3c), **b** prolate spheroids (Fig. 3b), **c** crossed spheroids (Fig. 3d), and **d** drilled oblate spheroids (Fig. 3e)

heterogeneity were established, one inclusion at a time. Subsequent inhomogeneities were added in such a way that they did not intersect the already fixed particles. If this was not possible at some point, the procedure was restarted with a new random distribution of centres. In the next step, the smallest distance between the surfaces of inclusions was numerically calculated, treating them as filled, i.e. ignoring the presence of hollows for some of the considered shapes, i.e. the drilled sphere (Fig. 3c) was treated as a sphere, and the drilled oblate spheroid (Fig. 3e) was regarded as an oblate spheroid. If the smallest distance between the surfaces of particles was less than 0.0005, the random structure was discarded to improve both accuracy and efficiency of later numerical calculations.

The above method of generating random structures is one of the simplest, but it proved to be sufficient for the purpose of the present studies. More advanced algorithms for three-dimensional random packing, which include an overlapping detection algorithm for an optimized simulation of the meso-structure, can be found in the literature, e.g. [40].

Let us demonstrate that the complexity of generating the required set of RVEs increases with the number of inclusions, especially if we aim to obtain a prescribed packing ratio for a given volume fraction. Fig. 7 presents normalized histograms of the packing ratio f_λ/f_m in random structures. Fig. 7a shows such histograms for spherical inclusions with a volume fraction of 30% and the number of particles in the RVE set to 10, 20 or 30. As the number of inclusions increases, the curve becomes narrower, i.e. to obtain several dozen structures with a similar value of the packing ratio within a given range, more trial microstructures are needed, e.g. for $f_\lambda/f_m = 0.03$, 10^6 random microstructures with 30 spherical inclusions were required to allow the selection of 30 RVEs with a similar packing ratio, i.e. $f_\lambda/f_m = 0.03 \pm 10^{-4}$.

Normalized histograms of f_λ/f_m for 30 particles with $f_i = 30\%$ and various shapes of inclusions (Fig. 3a–e) are shown in Fig. 7b. The drilled spheres, which have approximately the same size in each direction (Fig. 3c), have the smallest average packing ratio and the narrowest spread of its values. The drilled oblate spheroids are at the other end of the spectrum. Despite the cavity, they have the largest average packing ratio and the widest scatter.

4 Results

4.1 Concentration tensors

In this section, the numerical diluted concentration tensor $\mathbb{A}_i^{NDil}$, calculated using the described procedure, is verified against the analytical solution derived by Eshelby [6]. The case of a spheroidal inclusion with semi-axes (a, b, b) is analyzed, with the ratio $\frac{a}{b}$ ranging from 0.5 to 2 and with different ratios of the phases' Young's moduli E_i/E_m.

In Fig. 8a, the material parameters were taken as for ceramic particles embedded in a metal matrix (MMC, Table 1), and in Fig. 8b Poisson's ratios of the inhomogeneities and the matrix are the same as for the MMC, i.e. $\nu_i = 0.2$ and $\nu_m = 0.3$, while the ratio of Young's moduli E_i/E_m changes as shown on the X axis with $E_m = 75[GPa]$. Note that for the MMC of Table 1, $E_i/E_m \approx 5.33$. The components A_n, $n = 0, \ldots, 3$ and 12, of the spheroid concentration tensor $\mathbb{A}$ are defined in Appendix B [Eq. (B.1)], and calculated from Eq. (B.3). In Fig. 8, good agreement between numerical and analytical results is observed: A_2 and

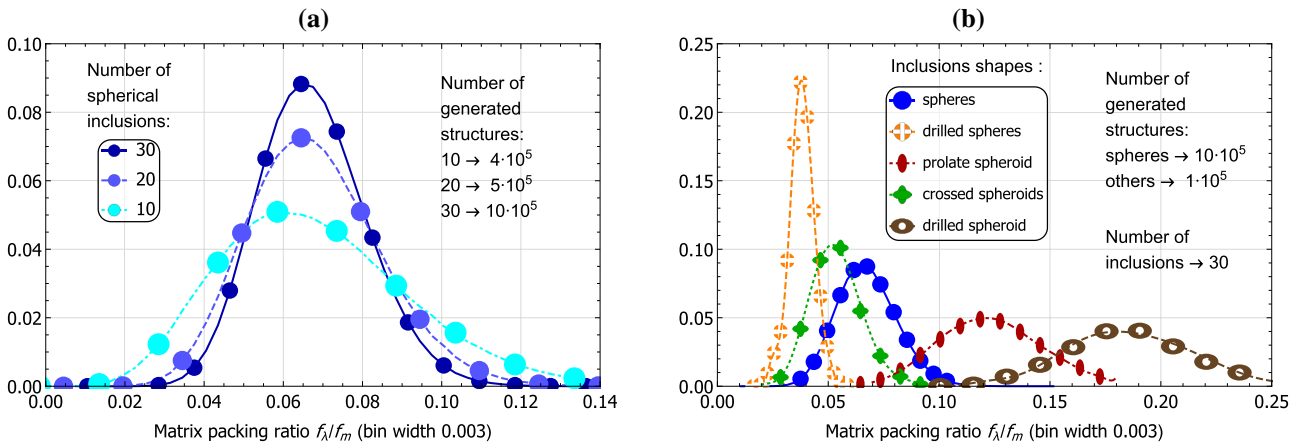

Fig. 7 Normalized histograms of the packing ratio f_λ/f_m for the volume fraction of inclusions 30% in random structures. **a** The number of spherical inhomogeneities is: 10, 20, or 30. **b** RVEs with 30 inhomogeneities of different shapes: spheres, prolate spheroids, drilled spheres, crossed spheroids and drilled spheroids (Fig. 3a–e, respectively)

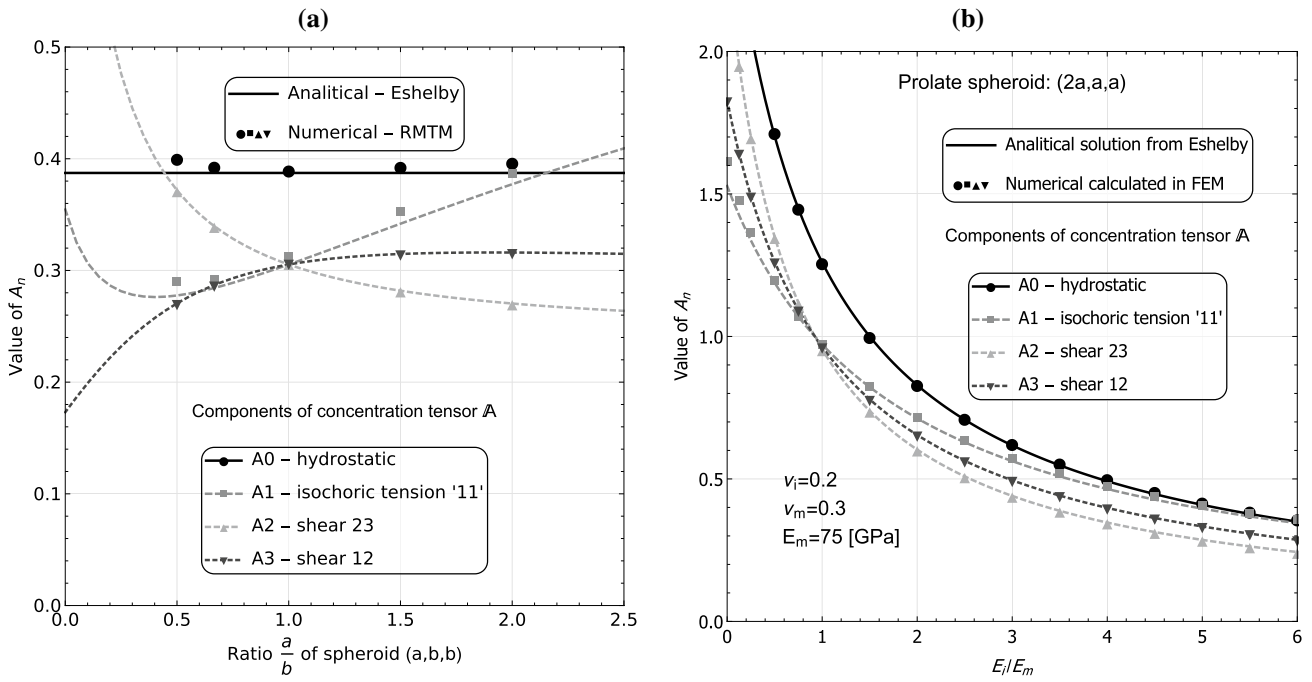

Fig. 8 Components of the spheroid concentration tensor $\mathbb{A}$ vs **a** the ratio of the spheroid's semi-axes $\frac{a}{b}$ for the MMC composite, **b** Young's moduli ratio between the material phases E_i/E_m for $\frac{a}{b} = 2$. Analitical results (lines) are from the Eshelby solution, numerical results—from the described RMTM procedure

Table 2 MMC components of the numerical $\mathbb{A}_i^{NDil}$ for different shapes: sphere, drilled sphere, prolate spheroid $a/b = 2$, crossed spheroids, and oblate spheroid $a/b = 2/3$ (Fig. 3a–e). The numerical dilute concentration tensors: $\mathbb{A}^{Iso}$—isotropy, $\mathbb{A}^{Cub}$—cubic anisotropy (Eq. B.2), $\mathbb{A}^{Trans}$—transverse anisotropy (Eq. B.1). The components A_n of $\mathbb{A}$ are listed in Appendix B.3

Symmetry of $\mathbb{A}$	Shape	A_0	A_1	A_2	A_3	A_{12}
$\mathbb{A}^{Iso}$	Sphere	0.387	0.306			–
$\mathbb{A}^{Cube}$	Drilled sphere	0.433	0.354	0.334		–
$\mathbb{A}^{Cube}$	Crossed spheroids	0.399	0.315	0.325		–
$\mathbb{A}^{Trans}$	Prolate spheroid	0.397	0.387	0.270	0.316	$\approx 10^{-2}$
$\mathbb{A}^{Trans}$	Drilled spheroid	0.401	0.335	0.298	0.345	$\approx 10^{-3}$

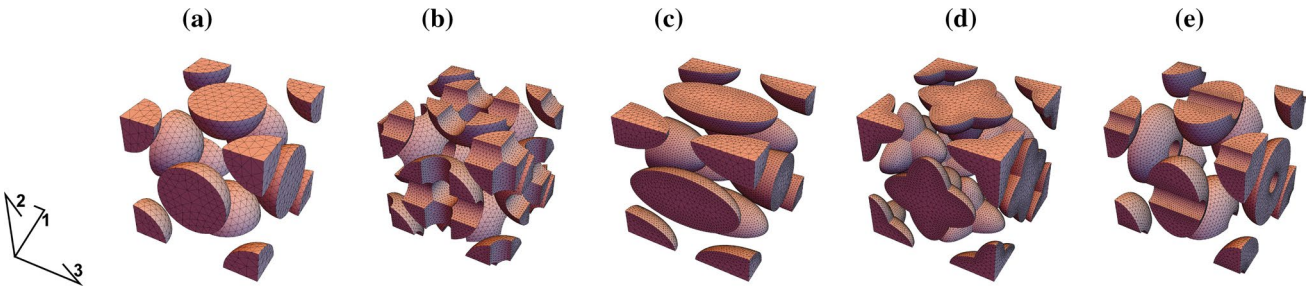

Fig. 9 UVEs with the FCC arragement of meshed inhomogeneities, $f_i = 30\%$: **a** spheres, **b** drilled spheres, **c** prolate spheroids, **d** crossed spheroids, and **e** drilled oblate spheroids. The matrix phase is not shown for clarity

A_3 predicted by both methods are almost the same (Fig. 8a), also numerical A_0 and A_1 lie close to the analytical results though a slight difference is visible here. As can be seen in Fig 8b, a change of contrast E_i/E_m does not worsen the agreement of results. Though the numerical A_{12} (Eq. B.3) equals 10^{-2} for $\frac{a}{b} = 2$, which is far smaller than the rest of the $\mathbb{A}$ components, the analytical A_{12} is almost 0 (around 10^{-5}). As expected, with increasing $E_i/E_m > 1$, the components of the concentration tensor decrease and take values smaller than one, which indicates a reduced capability of the inhomogeneity to accommodate the overall strain. The limit case would be a rigid inclusion which is not able to accommodate any strain. A reverse trend is observed for decreasing $E_i/E_m < 1$, in which case the soft inhomogeneity is more and more 'eager' to accommodate strain.

Table 2 contains the independent components of the numerical diluted concentration tensor $\mathbb{A}_i^{NDil}$ for different shapes of inhomogeneities, properties of which are given in Table 1. For a sphere $\mathbb{A}_i^{NDil}$ is isotropic, for the crossed spheroids and the drilled sphere it has cubic symmetry (see $\mathbb{A}^{Cub}$ in Eq. B.2), and for the prolate, oblate and drilled spheroid it is transversely isotropic (see $\mathbb{A}^{Trans}$ in Eq. B.1). Let us observe that the spherical component A_0 of $\mathbb{A}_i^{NDil}$ is similar for different shapes, but the components of the deviatoric part: A_1, A_2, and A_3 are sensitive to the shape change. Note that the value of component A_1 for the prolate spheroid is higher than for a sphere. This could be rationalized as follows. For the strain given by Eq. $(19)_2$, it is necessary to elongate the composite in the direction of the main axis of the spheroid. Thus, in this direction the inhomogeneity needs to participate more in the composite's strain. It can be clearly seen when we imagine infinitely long spheroids—fibres—which must accommodate the composite's total strain in their direction. On the other hand, this is not necessary when we consider the strain in the transverse direction. When comparing the components of $\mathbb{A}_i^{NDil}$ for a sphere with those for the drilled sphere, larger values of the components A_k are observed for the second shape. It means that in the second case more strain is accommodated by the inhomogeneity. It is worth recalling that the numerical strain concentration tensor $\mathbb{A}_i^{NDil}$ is calculated from the inhomogeneity's domain excluding the cavity if the inhomogeneity is drilled.

4.2 FCC arrangements of inclusions

In this section, effective material parameters of two-phase composites are discussed. It is assumed that the spatial distribution of inhomogeneities is the same as in the face-centred cubic crystal lattice. The arrangement of particles in the Unit Volume Element (UVE), which is a 1×1×1 cube, is shown in Fig. 9. The FE mesh for inclusions is presented in Fig. 9, where the matrix phase is hidden for better clarity of the figure. The mesh size was chosen so that the difference

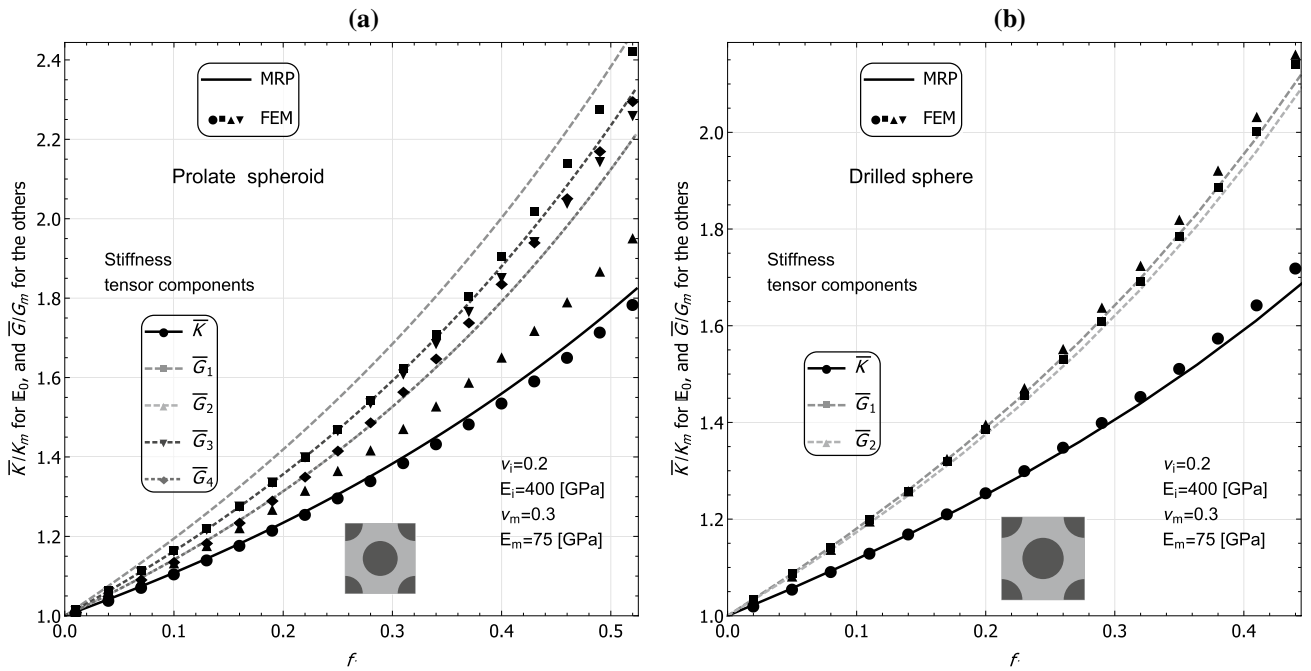

Fig. 10 The metal matrix composite (MMC) reinforced with ceramic particles arranged in the face-centred cubic (FCC) system. Components of the effective stiffness tensor **a** $\overline{\mathbb{L}}^{Tetra}$ (Eq. A.9) with prolate spheroids (2a,a,a) (Fig. 9c), and **b** $\overline{\mathbb{L}}^{Cub}$ (Eq. A.8) with drilled spheres (Fig. 9b) as inclusions. Notation: f_i the volume fraction of inclusions, *MRP* the MRP based on RMTM and MT* (Fig. 1), *FEM* numerical homogenization

in the obtained results is less than 1% after a subsequent mesh refinement. The assumed shapes of inhomogeneities are discussed in Sect. 2.2.

The influence of the inclusions' volume fraction f_i in the MMC (Tab. 1) on the effective properties is studied first. Fig. 10 demonstrates the effective stiffness tensor of: tetragonal symmetry $\overline{\mathbb{L}}^{Tetra}$ (Fig. 10a) for the UVE reinforced with prolate spheroids (Fig. 9c), and cubic symmetry $\overline{\mathbb{L}}^{Cub}$ (Fig. 10b) for the UVE reinforced with drilled spheres (Fig. 9b). The six independent components of $\overline{\mathbb{L}}^{Tetra}$ (Eq. A.9) are established by performing five numerical tests (Eq. 19 and Eq. A.12), and the three independent components of $\overline{\mathbb{L}}^{Cub}$ (Eq. A.8) are established by performing tests using $E_{ij}^{(0)}, E_{ij}^{(1)}$, and $E_{ij}^{(2)}$ from Eq. 19. Let us emphasize that the estimates of the MRP model are insensitive to the spatial distribution of inclusions, so the effective stiffness tensor obtained by this method inherits the symmetry group of the concentration tensor. Therefore, for the prolate spheroid it has transverse isotropy and the shear moduli $\bar{G}_2$ and $\bar{G}_4$ obtained by MRP, contrary to FEM results, are equal in Fig. 10a. This analytical outcome lies between the numerical homogenization results. The order of the macroscopic shear moduli estimated by MRP: $\bar{G}_1 > \bar{G}_2 > \bar{G}_3$ (Fig. 10a) corresponds to the order of the respective components of the numerical concentration tensor: $A_1 > A_2 > A_3$ (Table 2 prolate spheroid). For smaller volume fractions of the particles, $f_i < 0.15$, $\bar{G}_1$ is almost equal to $\bar{G}_3$, and $\bar{G}_2$ is close to $\bar{G}_4$ for FEM results. For the FCC MMC reinforced with ceramic drilled spheres (Fig. 10b), there is good agreement between the FEM and MRP results.

The influence of the inhomogeneity's shape on the effective properties is demonstrated next. Fig. 11 shows the effective shear modulus (a) $\overline{G}_1$ and (b) $\overline{G}_2$ of the UVE made of the MMC (Table 1) reinforced with ceramic particles in the FCC arrangement and having one of the five different shapes: sphere, drilled sphere, prolate spheroid, crossed spheroids, and drilled oblate spheroid (Fig. 3). Because the geometries of inclusions differ, the maximum volume fraction of inhomogeneities in the FCC system varies. The order of the macroscopic shear moduli G_1 and G_2 by MRP in Fig. 11 corresponds to the order of the first (Fig. 11a) and second (Fig. 11b) component of $\mathbb{A}_i^{NDil}$ (Table 2) for the different shapes as, under the loading conditions $\mathbf{E}_1$ and $\mathbf{E}_2$, respectively, more strain is accommodated by the stiffer inhomogeneity phase. The MRP estimates and results of numerical homogenization are in good agreement except for the case of the prolate spheroids (Fig. 11). This discrepancy follows from the tetragonal symmetry of the FCC UVE, which is not accounted for by the MRP scheme. In general, the metal matrix composite is the stiffest in terms of the considered component of the elasticity tensor when it is reinforced with the ceramic spheroids drilled in three directions. The biggest difference

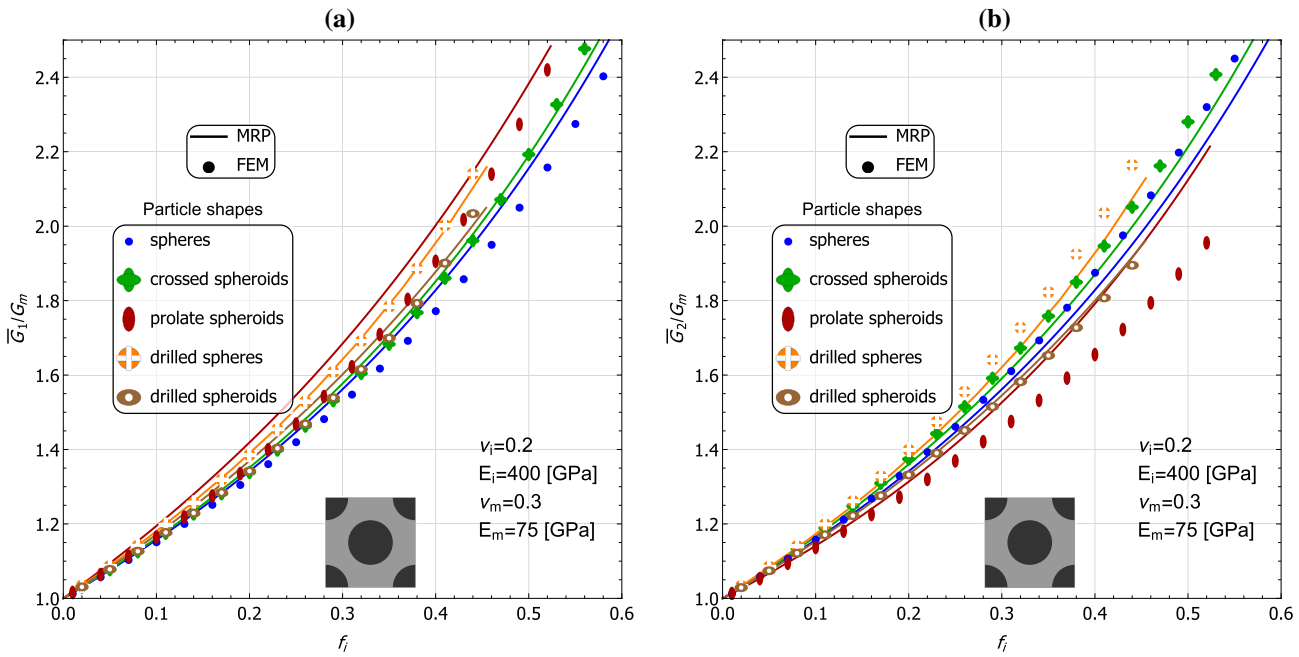

Fig. 11 The metal matrix composite (MMC) reinforced with ceramic particles arranged in the face-centred cubic (FCC) system. The effective shear modulus **a** $\overline{G}_1$ for $\mathbf{E}^{(1)}$, and **b** $\overline{G}_2$ for $\mathbf{E}^{(2)}$ in BC (Eq. A.12) for different shapes of inhomogeneities (Fig. 3). Notation: f_i the volume fraction of inclusions, *MRP* the MRP based on RMTM and MT* (Fig. 1), *FEM* numerical homogenization

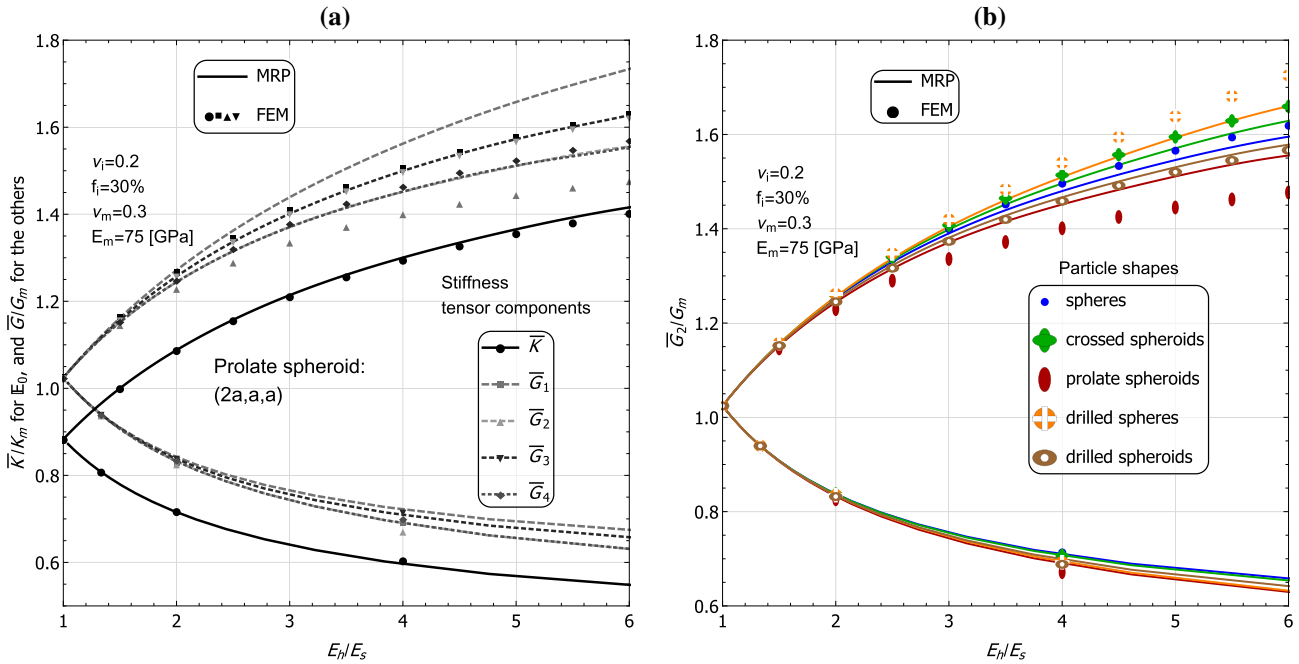

Fig. 12 Two-phase composite with a varying ratio E_i/E_m ($\nu_i = 0.2$, $\nu_m = 0.3$), particles placed according to the face-centred cubic (FCC) system, two configurations: $(E_h, E_s) = (E_i, E_m)$ or $(E_h, E_s) = (E_m, E_i)$. (a) Components of the effective stiffness tensor $\overline{\mathbb{L}}^{Tetra}$ (Eq. A.9) for prolate spheroids with axes $(2a, a, a)$ (Fig. 9.c). (b) The effective shear modulus $\overline{G}_2$ for $\mathbf{E}^{(2)}$ in BC (Eq. A.12) for different shapes of inhomogeneities (Fig. 3). Notation: *MRP* the MRP based on RMTM and MT* (Fig. 1), *FEM* numerical homogenization

between the effective stiffness G_1 and G_2 (Fig. 11a and b) is for spheroids: prolate and drilled.

Second, the influence of contrast in the elastic properties of phases, i.e. the ratio E_i/E_m between the Young's moduli of the inclusions and matrix, is studied for the fixed volume fraction of inclusions $f_i = 0.3$. Because the material parameters change, the numerical concentration tensor is calculated independently for each value of E_i/E_m. Fig. 12 shows $\bar{K}$ and four $\bar{G}$ as a function of the Young's moduli ratio between the hard and soft phase, E_h/E_s. The curves in the upper part of Fig. 12 have $E_i > E_m$, so $E_i = E_h$, and in the lower part $E_i < E_m$, thus $E_i = E_s$. Fig. 12a demonstrates the independent components of the effective elasticity tensor $\overline{\mathbb{L}}^{Tetra}$ of the UVE reinforced with prolate spheroids with semi-axes $(2a, a, a)$ (Fig. 9c). As before, the biggest difference between the numerical and MRP model predictions is seen for the $\bar{G}_1$ and $\bar{G}_2$ elastic constants. For the remaining shapes of particles, good agreement was found as demonstrated in Fig. 12b using the example of the $\bar{G}_2$ modulus. Overall, effective properties of UVEs with inhomogeneities of cubic symmetry described by $\mathbb{A}^{Cub}$ estimated by MRP are in better agreement with numerical results because these inclusions have the same symmetry as the FCC spatial distribution of particles. The varying contrast in phase properties does not significantly change the consistency of agreement between the MRP and numerical predictions.

4.3 Random arrangements of inclusions

In this section, macroscopic material parameters of two-phase composites with randomly distributed particles are considered, and the packing effects are studied. To investigate the impact of the packing ratio f_λ/f_m on the effective behaviour of particulate composites, at least 10^5 random microstructures were generated to select 30 RVEs with a similar packing ratio to a tolerance of $\pm 10^{-4}$.

In Fig. 13, the effective material parameters: (a) bulk $\overline{K}$, and (b) shear $\overline{G}$ modulus are shown vs the packing ratio f_λ/f_m of the MMC reinforced with ceramic particles of the five different shapes. Numerical homogenization was performed by FEM and lasted around 1 h for the assumed mesh size. The mesh size was such that a subsequent mesh refinement gave a difference in the effective bulk and shear moduli, respectively, of less than 2%. In Fig. 13, the boundary conditions for the FEM calculations of $\overline{K}$ and $\overline{G}$ were specified by $\mathbf{E}^{(0)}$ and $\mathbf{E}^{(1)}$ (Eq. 19), respectively. Each point of the FEM results corresponds to simulations of 30 random structures with almost identical packing parameters f_λ/f_m. Triangles mark the 95% confidence interval for the population mean, and the shape symbol marks the average over all 30 random structures. Because among the generated random structures the range of the packing ratio f_λ/f_m is narrow (see Fig. 7b) for the drilled spheres and the crossed spheroids, it was decided to

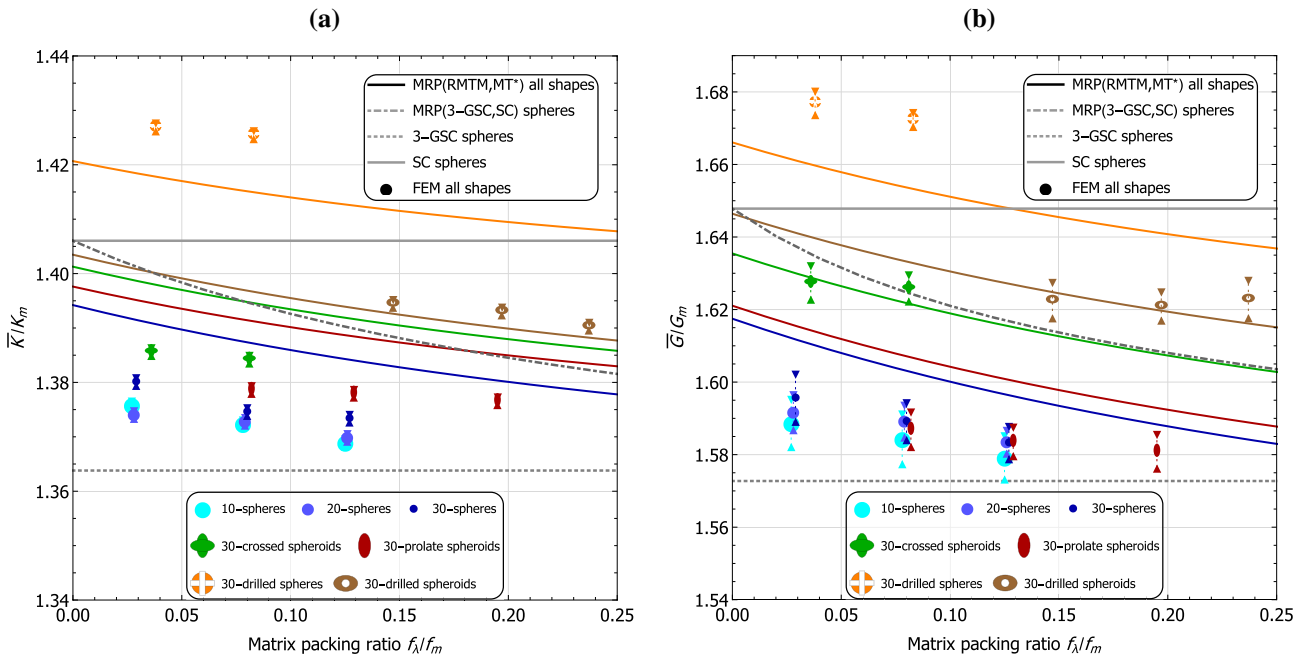

Fig. 13 Two-phase composite (Table 1) with a continuous metal matrix and different shapes of 30 randomly oriented ceramic inhomogeneities (Fig. 3a–f) with $f_i = 0.3$. The effective **a** bulk modulus $\overline{K}$ and (b) shear modulus $\overline{G}$, scaled by matrix parameters, vs the packing ratio f_λ/f_m. Notation: *MRP (RMTM,MT*)* the present MRP model based on the RMTM and MT* patterns (Fig. 1), *FEM* numerical homogenization. Each FEM mark (e.g. dots for spheres) denotes the mean of 30 random RVEs of the same f_λ/f_m; triangles mark the 95% confidence interval for the population mean

take only two representative packing parameters (Fig. 13) for these shapes. It can be seen that the macroscopic bulk modulus (Fig. 13a) has a smaller spread than the effective shear modulus (Fig. 13b). This feature conforms with the results reported in [11]. Moreover, the packing ratio f_λ/f_m affects the effective material parameters, but the impact is small compared to the effect of shape, at least in the considered elastic range. However, as it was shown in the paper [13], the packing ratio plays a major role in the non-elastic response of composites, e.g. in plasticity.

RVEs of particulate composites with randomly distributed and oriented inclusions are isotropic. In this research, 30 particles were enough to obtain similar shear moduli for all deviatoric tests (Eq. A.12). Because the numerical concentration tensors have the same symmetry as the inclusion shapes, an isotropization procedure was used. For all shapes, the effective shear modulus $\bar{G}$ was taken as a weighted average of all calculated $\bar{G}_k$ [11]. The MRP model predicts a trend similar to the numerical outcomes for the influence of the packing ratio on effective stiffness parameters. Slight stiffening of the material is predicted when the packing parameter decreases, with the effective response of the composite reinforced with drilled spheres being the stiffest, as for the FCC MMC studied in Fig. 11. The effective shear moduli

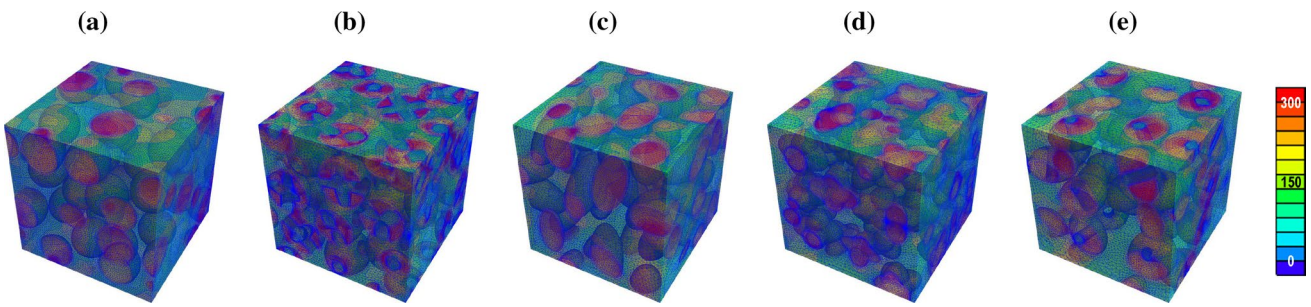

Fig. 14 Equivalent von Mises stress (legend 0–300 MPa, the same for all plots) within periodic representative volume elements of random composites, each containing 30 inclusions with a volume fraction of 30%. The shapes of inclusions are: **a** spheres, **b** drilled spheres (Fig. 3c), **c** prolate spheroids (Fig. 3b), **d** crossed spheroids (Fig. 3d), and **e** drilled oblate spheroids (Fig. 3e)

$\bar{G}$ obtained by numerical homogenization for drilled spheroids and crossed spheroids are similar (Fig. 13b), despite the different packing ratios.

In Fig. 14, the Mises stress contour maps for selected microstructures (Fig. 6) are presented. As can be seen, the equivalent stress level within the matrix phase inside drilled inhomogeneities is smaller than in the surrounding matrix, because stiff ceramic particles prevent the development of higher strains in these areas. In Fig. 14, the maximum von Mises stress in each representative volume ranges from 793 for spheres (Fig. 14a), to 1840 MPa for crossed spheroids (Fig. 14d), to 2992 MPa for prolate spheroids (Fig. 14c), to 5290 MPa for drilled spheres (Fig. 14b), to 6820 MPa for drilled oblate spheroids (Fig. 14.e). These results were obtained for these particular realizations of the representative volumes and do not necessarily represent values found for the whole range of the random composites. Nevertheless, they are listed to help interpret the contour maps in Fig. 14.

5 Conclusions

This study investigated the effects of particle packing and shape on the overall elastic properties of particulate composites using the mean-field morphologically representative pattern approach. In the MRP approach, the composite microstructure was represented by two patterns: the replacement Mori–Tanaka model and a Mori–Tanaka-type (MT*) estimate. The RMTM pattern comprised a composite inclusion composed of an inclusion surrounded by two coatings: the first one specified by the minimum distances λ_k between particles in the representative volume, the second one by the volume fraction of inclusions and of the matrix outside the λ-coatings region. Thus, the parameters describing the packing of the particles were minimum distances between particles. The RMTM was used to account for the shape effect because it allows one to numerically estimate the effective response of any shape of inclusion. The MT* pattern, containing the remaining matrix material surrounded by a medium with the effective parameters of the composite inclusion, takes into account interactions between composite inclusions.

The analytical mean-field models were confronted with the results of computational homogenization performed using the finite element method. Samples with both regular and random arrangements of particles were generated. Representative volume elements with random distributions of 10, 20, or 30 particles, and periodic unit cells with face-centred cubic crystal-type arrangements were used. In the RVE's case, to isotropize the anisotropic MRP estimates of the effective stiffness tensor for a single non-spherical inhomogeneity, a method was proposed that treats the composite material as a polycrystal made of randomly oriented domains corresponding to the unit cells.

The MRP-based assessments of the influence of the inhomogeneities' shape and packing on the macroscopic behaviour of particulate composites were verified by performing numerical simulations. The MRP approach predicts a stronger stiffening effect of the decreasing minimum distance between reinforcement particles on the overall response compared to the FEM results. However, quantitatively the MRP elastic moduli are lower than those obtained using FE homogenization for FCC unit volumes, especially for high volume contents of inclusions, approaching a limit when particles are in contact. MRP is based on numerical concentration tensors calculated for the dilute volume fraction of a single inhomogeneity, so the estimates of the MRP model are insensitive to the spatial arrangement of inclusions. Therefore, the FEM and MRP results for FCC volumes are not in agreement for higher volume fractions of inclusions.

Both the MRP and FEM results predict a strong impact of the shape of particles on the effective properties. Five selected shapes of inhomogeneities were considered in the article: a sphere, a prolate spheroid, a sphere with three perpendicular cylindrical cavities (drilled sphere), three prolate spheroids crossing at right angles (crossed spheroids), and an oblate spheroid with a cylindrical cavity (drilled oblate spheroid). As concerns qualitative predictions related to packing in such cases, similar trends as those observed for two-phase composites reinforced with spherical inclusions can be seen. The tendencies predicted by MRP are consistent with FEM results in the case of all studied shapes—an especially good agreement was obtained for drilled oblate spheroids. In the case of highly irregular shapes of the particles, the numerical simulations of the concentration tensor could be more challenging. Especially when there is significant unevenness of the surface of the particle, which makes mesh quality an important factor. On the other hand, it is substantially easier to simulate single irregular inhomogeneities than an RVE with many irregular inclusions.

One may conclude from the presented studies that MRP estimates, by accounting for particle shapes and packing, may improve classical micromechanical estimates in the case of moderate volume contents. The inclusions' shape can be used as a design parameter to be found using the multi-objective optimization procedure presented in [41]. Additionally, it is foreseen that this approach may be particularly useful with respect to particulate composites in the elastic–plastic regime or with damage evolution. Therefore, an extension of the presented MRP approach to the non-linear regime is a subject of our current research. The extension can be performed by applying the concept of incremental linearization of elastic–plastic constitutive relations proposed by Hill [42], like it was done in our recent paper [13].

Such linearization is obtained by adopting either tangent or secant material moduli [42]. Therefore, the use of the RMTM and MT* formalism requires isotropization of the current moduli, which are usually anisotropic [14]. To this end, the algorithm for microstructure generation presented in this paper can be directly applied. The correctness of the choice of either modulus can be verified numerically.

Our preliminary studies using a simple continuum damage model presented in 8 enable us to hypothesize about basic trends in material degradation related to different shapes and spatial distributions of particles. On the basis of these observations, some guidelines for building an efficient analytical or semi-analytical model incorporating damage may be formulated. In general, more localized damage is observed in the case of a smaller distance between the particles' outer surfaces and more spherical shapes of inclusions. In short, the proposed damage will be developed until fracture of the material. To improve the MRP model's predictions each inclusion will be considered separately, as schematically shown in Fig. 15

Appendix A: Stiffness tensor decompositions: transverse isotropy and cubic symmetry

In the paper, five different shapes are studied (see Fig. 3a–e). Let us assume that the spheroid is prolate (Fig. 3c) or oblate and drilled (Fig. 3e) in the $\mathbf{m}_1$ direction. Then the stiffness tensor $\overline{\mathbb{L}}_i^{dil}$ of a tiny spheroid embedded in a large cube (Fig. 4) and the effective stiffness tensor $\overline{\mathbb{L}}_{NDil}$ in Eq. 14 exhibit transverse isotropy and can be written in the following form [43]:

$$\begin{aligned}\overline{\mathbb{L}}^{Trans} =& 3\overline{K}\mathbb{I}^P + 2\overline{G}_1\mathbb{P}_1 + 2\overline{G}_2\mathbb{P}_2 + 2\overline{G}_3\mathbb{P}_3 \\ &+ 2\overline{G}_{12}\frac{1}{\sqrt{6}}(\mathbf{d}\otimes\mathbf{I} + \mathbf{I}\otimes\mathbf{d})\,.\end{aligned} \tag{A.1}$$

The orthogonal projectors $\mathbb{P}_K$ $(K = 1, 2, 3)$ define:

- 1D space of isochoric tension/compression along $\mathbf{m}_1$

$$\mathbb{P}_1 = \mathbf{d}\otimes\mathbf{d}\,, \quad \mathbf{d} = \frac{1}{\sqrt{6}}\left(3\mathbf{m}_1\otimes\mathbf{m}_1 - \mathbf{I}\right), \tag{A.2}$$

- 2D space of in-plane shears

$$\begin{aligned}\mathbb{P}_2 =& \frac{1}{2}\left[(\mathbf{m}_2\otimes\mathbf{m}_3 + \mathbf{m}_3\otimes\mathbf{m}_2)\otimes(\mathbf{m}_2\otimes\mathbf{m}_3 + \mathbf{m}_3\otimes\mathbf{m}_2)\right. \\ &\left.+(\mathbf{m}_2\otimes\mathbf{m}_2 - \mathbf{m}_3\otimes\mathbf{m}_3)\otimes(\mathbf{m}_3\otimes\mathbf{m}_3 - \mathbf{m}_2\otimes\mathbf{m}_2)\right],\end{aligned} \tag{A.3}$$

- 2D space of out-of-plane shears where

$$\mathbb{P}_3 = \frac{1}{2}\sum_{k=2,3}\left(\mathbf{m}_1\otimes\mathbf{m}_k + \mathbf{m}_k\otimes\mathbf{m}_1\right)\otimes\left(\mathbf{m}_1\otimes\mathbf{m}_k + \mathbf{m}_k\otimes\mathbf{m}_1\right). \tag{A.4}$$

As it was mentioned, to calculate the five independent components: $3\overline{K}, 2\overline{G}_1, 2\overline{G}_{12}, 2\overline{G}_2, 2\overline{G}_3$, a set of four analyses with micro-periodic displacement boundary conditions (Eq. 16) were performed for a unit volume element. The four strain tensors $\mathbf{E}^{(n)}$ $(n = 0, 1, 2, 3)$ imposed in these analyses are given by Eq. (19).

The strains $\mathbf{E}^{(n)}$ result in the overall stresses, calculated as the local stresses averaged over the RVE's volume, $\mathbf{\Sigma}^{(n)} = 1/V\int_V \boldsymbol{\sigma}dV$, which allow one to derive each independent component of $\overline{\mathbb{L}}^{Trans}$ according to the relations:

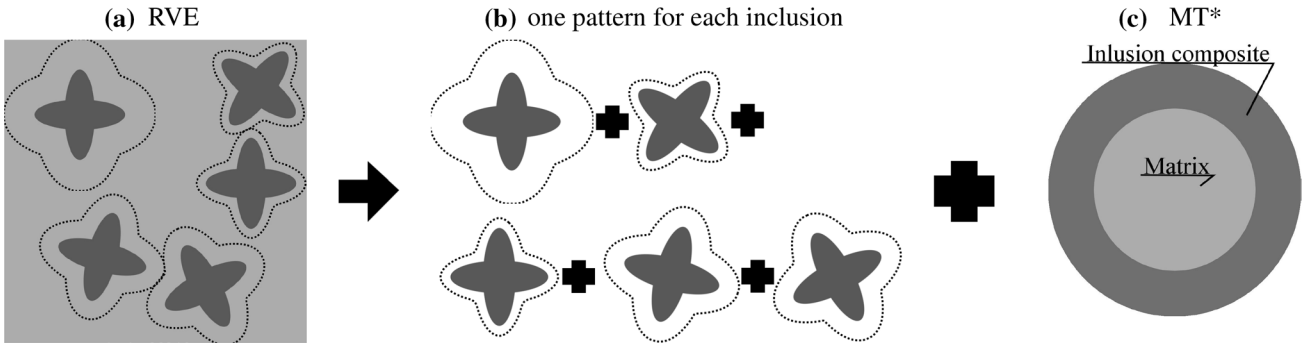

Fig. 15 The microstructure of a two-phase composite reinforced with five inclusions represented in the MRP approach by six patterns: **b** each inclusion represented by its own pattern and **c** the MT* pattern

$$3\overline{K} = \frac{\Sigma_{11}^{(0)} + 2\Sigma_{22}^{(0)}}{3d}, \quad 2\overline{G}_{12} = \frac{\Sigma_{11}^{(0)} - \Sigma_{22}^{(0)} + \Sigma_{11}^{(1)} + 2\Sigma_{22}^{(1)}}{3d},$$
$$2\overline{G}_1 = \frac{2\left(\Sigma_{11}^{(1)} - \Sigma_{22}^{(1)}\right)}{3d}, \quad 2\overline{G}_2 = \frac{\Sigma_{23}^{(2)}}{d}, \quad 2\overline{G}_3 = \frac{\Sigma_{12}^{(3)}}{d}, \tag{A.5}$$

where $\Sigma_{ij}^{(n)}$ denotes the ij component of the averaged stress tensor $\boldsymbol{\Sigma}^{(n)}$ obtained as a material response to the strain $\mathbf{E}^{(n)}$.

For the other shapes, i.e. the drilled sphere and crossed spheroids (Fig. 3c and d), the effective elastic stiffness tensor $\overline{\mathbb{L}}^{Cub}$ of the unit cells is the anisotropic fourth-order tensor relevant for cubic symmetry with three Kelvin moduli $3\overline{K}$, $2\overline{G}_1$, and $2\overline{G}_2$, namely [38]:

$$\overline{\mathbb{L}}^{Cub} = 3\overline{K}\mathbb{I}^{\mathrm{P}} + 2\overline{G}_1(\mathbb{K} - \mathbb{I}^P) + 2\overline{G}_2(\mathbb{I} - \mathbb{K}), \tag{A.6}$$

where

$$\mathbb{K} = \sum_{k=1}^{3} \mathbf{m}_k \otimes \mathbf{m}_k \otimes \mathbf{m}_k \otimes \mathbf{m}_k, \quad \mathbb{I}^P = \frac{1}{3}\mathbf{I} \otimes \mathbf{I}, \tag{A.7}$$

and $\mathbf{m}_k$ are the main symmetry axes of the unit cell. The eigensubspaces corresponding to $3\overline{K}$, $2\overline{G}_1$, and $2\overline{G}_2$ are one dimensional (the space of hydrostatic states), two dimensional, and three dimensional (two orthogonal subspaces of deviatoric states), respectively.

Only three FE analyses with strains $\mathbf{E}^{(0)}$, $\mathbf{E}^{(1)}$, and $\mathbf{E}^{(2)}$ imposed by periodic boundary conditions (Eq. 19) are needed to derive each Kelvin modulus independently, according to the relations:

$$3\overline{K} = \frac{\boldsymbol{\Sigma}_{11}^{(0)}}{d}, \quad 2\overline{G}_1 = \frac{\boldsymbol{\Sigma}_{11}^{(1)}}{d}, \quad 2\overline{G}_2 = \frac{\boldsymbol{\Sigma}_{23}^{(2)}}{d}. \tag{A.8}$$

It can be seen that the above three strains $\mathbf{E}^{(0)}$, $\mathbf{E}^{(1)}$, and $\mathbf{E}^{(2)}$ belong to three distinct eigensubspaces of the tensor $\overline{\mathbb{L}}^{Cub}$ and result in the overall stresses $\boldsymbol{\Sigma}^{(0)}$, $\boldsymbol{\Sigma}^{(1)}$, and $\boldsymbol{\Sigma}^{(2)}$ of the same structure as strains. Finally, the response of a unit volume element reinforced with a single tiny spherical inhomogeneity (Fig. 4) is isotropic.

The situation changes in the case of unit cells with the FCC placement of inhomogeneities (Fig. 9), which for spherical inclusions are of cubic symmetry. If the composite is reinforced with prolate (Fig. 9c) or oblate (Fig. 9e) spheroids, the effective stiffness tensor $\overline{\mathbb{L}}$ has tetragonal symmetry and can be written in the following form:

$$\begin{aligned}\overline{\mathbb{L}}^{Tetra} =& 3\overline{K}\mathbb{I}^P + 2\overline{G}_1\mathbb{P}_1 + 2\overline{G}_2\hat{\mathbb{P}}_2 + 2\overline{G}_3\mathbb{P}_3 \\ &+ 2\overline{G}_4\hat{\mathbb{P}}_4 + 2\overline{G}_{12}\frac{1}{\sqrt{6}}(\mathbf{d} \otimes \mathbf{I} + \mathbf{I} \otimes \mathbf{d}),\end{aligned} \tag{A.9}$$

where $3\overline{K}$, $2\overline{G}_1$, $2\overline{G}_{12}$, $2\overline{G}_2$, $2\overline{G}_3$, $2\overline{G}_4$ are six independent components. Note that it is assumed that the main axis of a prolate or oblate spheroid, or a drilled sphere, is coaxial with the $\mathbf{m}_1$ direction, which is at the same time coaxial with one of the unit cell's edges $\mathbf{m}_k$. Under such conditions, the projectors $\mathbb{P}_K$ (K=1,3) for tetragonal symmetry are the same as for the transversal one. The projectors $\hat{\mathbb{P}}_2$ and $\hat{\mathbb{P}}_4$ sum up to $\mathbb{P}_2$ for transverse isotropy. They define two 1D orthogonal subspaces of shearing in the 2–3 plane, namely:

- pure shear along the $\mathbf{m}_2$ and $\mathbf{m}_3$ directions,

$$\hat{\mathbb{P}}_2 = \frac{1}{2}\left[(\mathbf{m}_2 \otimes \mathbf{m}_3 + \mathbf{m}_3 \otimes \mathbf{m}_2) \otimes (\mathbf{m}_2 \otimes \mathbf{m}_3 + \mathbf{m}_3 \otimes \mathbf{m}_2)\right], \tag{A.10}$$

- pure shear along directions inclined by 45^o with respect to the $\mathbf{m}_2$ and $\mathbf{m}_3$ directions,

$$\hat{\mathbb{P}}_4 = \frac{1}{2}\left[(\mathbf{m}_2 \otimes \mathbf{m}_2 - \mathbf{m}_3 \otimes \mathbf{m}_3) \otimes (\mathbf{m}_3 \otimes \mathbf{m}_3 - \mathbf{m}_2 \otimes \mathbf{m}_2)\right]. \tag{A.11}$$

To find the six independent components of $\overline{\mathbb{L}}^{Tetra}$, the four analyses with the overall strains $\mathbf{E}^{(n)}$ ($n = 0, 1, 2, 3$) given by Eqs. (19), performed in the case of the overall transverse isotropy, are completed with a fifth analysis with an imposed strain of the following representation in the basis $\{\mathbf{m}_i\}$:

$$E_{ij}^{(4)} = \begin{pmatrix} 0 & 0 & 0 \\ 0 & d & 0 \\ 0 & 0 & -d \end{pmatrix}, \tag{A.12}$$

where d specifies the strain magnitude.

The imposed strains $\mathbf{E}^{(n)}$ result in the overall stresses $\boldsymbol{\Sigma}^{(n)}$, which allow one to derive each independent component of $\overline{\mathbb{L}}^{Tetra}$ according to Eq. A.5 with the addition of $\overline{G}_4$:

$$2\overline{G}_4 = \frac{\boldsymbol{\Sigma}_{22}^{(4)}}{d}. \tag{A.13}$$

The effective stiffness of a composite with the FCC arrangement of inhomogeneities shown in Fig. 9a, b and d is of cubic symmetry as long as the main axes of ingomogeneities coincide with the axes of the unit cell.

Appendix B: The form of concentration tensors: transverse isotropy and cubic symmetry

The numerical strain concentration tensor $\mathbb{A}_i^{NDil}$ of an inhomogeneity has the same symmetry group as the effective stiffness tensor of a large unit cell (Fig. 4) with a tiny inhomogeneity. Thus, for inhomogeneities having the shape of the prolate

spheroid or drilled oblate spheroid (Fig. 3b and e) its symmetry group is that for transverse isotropy:

$$\begin{aligned}\mathbb{A}^{Trans} =& A_0^{Trans}\mathbb{I}^P + A_1^{Trans}\mathbb{P}_1 + A_2^{Trans}\mathbb{P}_2 + A_3^{Trans}\mathbb{P}_3 \\ &+ \frac{1}{\sqrt{6}}\left(A_{12}^{Trans}\mathbf{d}\otimes\mathbf{I} + A_{21}^{Trans}\mathbf{I}\otimes\mathbf{d}\right),\end{aligned} \tag{B.1}$$

and for the other shapes: drilled sphere and crossed spheroids (Fig. 3c and d), it has cubic symmetry, viz.

$$\mathbb{A}^{Cub} = A_0^{Cub}\mathbb{I}^{\mathrm{P}} + A_1^{Cub}(\mathbb{K} - \mathbb{I}^P) + A_2^{Cub}(\mathbb{I} - \mathbb{K}), \tag{B.2}$$

where the projectors $\mathbb{P}_K$ and the remaining tensorial quantities, e.g. $\mathbb{K}$, are listed above; see Eqs. A.2, A.3, and A.7. Finally, if a particle is spherical then the numerical strain concentration tensor is isotropic.

For the set of micro-periodic displacement boundary conditions specified by the strains $\mathbf{E}^{(n)}$ from Eq. (19), the components A^{Cub} and A^{Trans}, established from Eq. (15), are:

$$\begin{aligned}
A_0^{Trans} &= \frac{\langle\boldsymbol{\varepsilon}\rangle_{11}^{(0)} + 2\langle\boldsymbol{\varepsilon}\rangle_{22}^{(0)}}{3d}, \quad A_{12}^{Trans} \approx \\
A_{21}^{Trans} &= \frac{\langle\boldsymbol{\varepsilon}\rangle_{11}^{(0)} - \langle\boldsymbol{\varepsilon}\rangle_{22}^{(0)} + \langle\boldsymbol{\varepsilon}\rangle_{11}^{(1)} + 2\langle\boldsymbol{\varepsilon}\rangle_{22}^{(1)}}{3d}, \\
A_1^{Trans} &= \frac{2\left(\langle\boldsymbol{\varepsilon}\rangle_{11}^{(1)} - \langle\boldsymbol{\varepsilon}\rangle_{22}^{(1)}\right)}{3d}, \\
A_2^{Trans} &= \frac{\langle\boldsymbol{\varepsilon}\rangle_{23}^{(2)}}{d}, \quad A_3^{Trans} = \frac{\langle\boldsymbol{\varepsilon}\rangle_{12}^{(3)}}{d}, \\
A_0^{Cub} &= \frac{\langle\boldsymbol{\varepsilon}\rangle_{11}^{(0)}}{d}, \quad A_1^{Cub} = \frac{\langle\boldsymbol{\varepsilon}\rangle_{11}^{(1)}}{d}, \quad A_2^{Cub} = \frac{\langle\boldsymbol{\varepsilon}\rangle_{23}^{(2)}}{d},
\end{aligned} \tag{B.3}$$

where $\langle\cdot\rangle$ is the volume averaging operation defined as $1/V\int_V(\cdot)dV$, $\boldsymbol{\varepsilon}$ is the local strain tensor in the inhomogeneity domain, $\langle\boldsymbol{\varepsilon}\rangle_{ij}^{(n)}$ is the component ij of the inhomogeneity's average strain in response to the displacement BC given by $\mathbf{E}^{(n)}$. The simplification $A_{12}^{Trans} \approx A_{21}^{Trans}$ was assumed taking into account very small values of this component compared to the remaining ones (see Table 2).

Appendix C: The impact of inclusion shape on damage evolution

As it has been shown, the shape of inclusions may substantially influence the local strain and stress fields in the composite phases. These local fields have a prominent effect on the initiation of damage in the material [20]. Below, we analyze damage evolution in composites with the considered shapes of heterogeneities by means of numerical homogenization.

Material degradation is simulated by FEM using the concept of the damage parameter d and the framework of continuous damage mechanics [44]. Within the local constitutive model of the phases, the free energy density Π is postulated in the form

$$\Pi = (1-d)\Pi_e(\boldsymbol{\varepsilon}), \tag{C.1}$$

where Π_e is the elastic energy density specified as

$$\Pi_e = \frac{1}{2}\boldsymbol{\varepsilon}\cdot\mathbb{L}_{i/m}\cdot\boldsymbol{\varepsilon}. \tag{C.2}$$

The damage parameter d depends on the history parameter ω which is related to the elastic energy density according to the exponential law [45]:

$$d = d_{max}(1 - Exp[-H\omega]), \tag{C.3}$$

where $d_{max} = 0.8$ is taken as the maximum damage, $H = 0.1$ is the damage ductility, and ω is equal to the maximum value of the elastic energy density Π_e achieved during the deformation process up to the considered time step.

Figure 16a presents the average value of the von Mises stress, calculated from the effective stress $\bar{\sigma}$, versus the overall strain component ε_{23} of the MMC (Table 1) subjected to periodic boundary conditions (16) with $\mathbf{E} = \mathbf{E}^{(2)}$. Similarly to [46], damage evolution is enabled only in the matrix phase. Figure 16b shows the average damage evolution $d_m = 1/V_m\int d\,dV_m$ in the matrix phase for five different inclusion shapes in the FCC spatial arrangement. The studied microstructures are presented in Fig. 9.

The results indicate that the shape of inhomogeneities plays a critical role in the non-linear response of the particulate composite. As can be seen in Fig. 16a, the difference in the overall von Mises stress between the crossed spheroids and the prolate spheroids is almost 500[MPa]. In all cases we observe first an increase in the stresses accompanied by a smooth reduction of stiffness. Next, some stabilization of the stress level is seen, so the strain increases under an approximately constant stress. Finally, the overall stresses start to increase again. The reason for this behaviour is the damage evolution law (Eq. C.1) and the assumption of the maximum damage $d_{max} = 0.8$ which is less than 1.0, so the elastic stiffness of the matrix never degrades to zero. When d reaches its maximum value d_{max}, the locally damaged matrix becomes elastic but with a smaller stiffness: $(1 - d_{max})\mathbb{L}_m$. The contour maps shown in Fig. 17 present the distribution of the damage parameter d at $\overline{\varepsilon}_{23} = 0.02$. Details of the distribution vary with the inclusion shape. In the MMC reinforced with prolate spheroids, wide and almost straight damage bands develop (see Fig. 17c), while for crossed spheroids damage bands are more curved (see Fig. 17d), and for drilled spheres damage develops in the matrix inside the inclusions (see Fig. 17b). In general, higher damage localization is observed in specimens with a smaller distance between the particles' external surfaces and with more spherical shapes of inclusions.

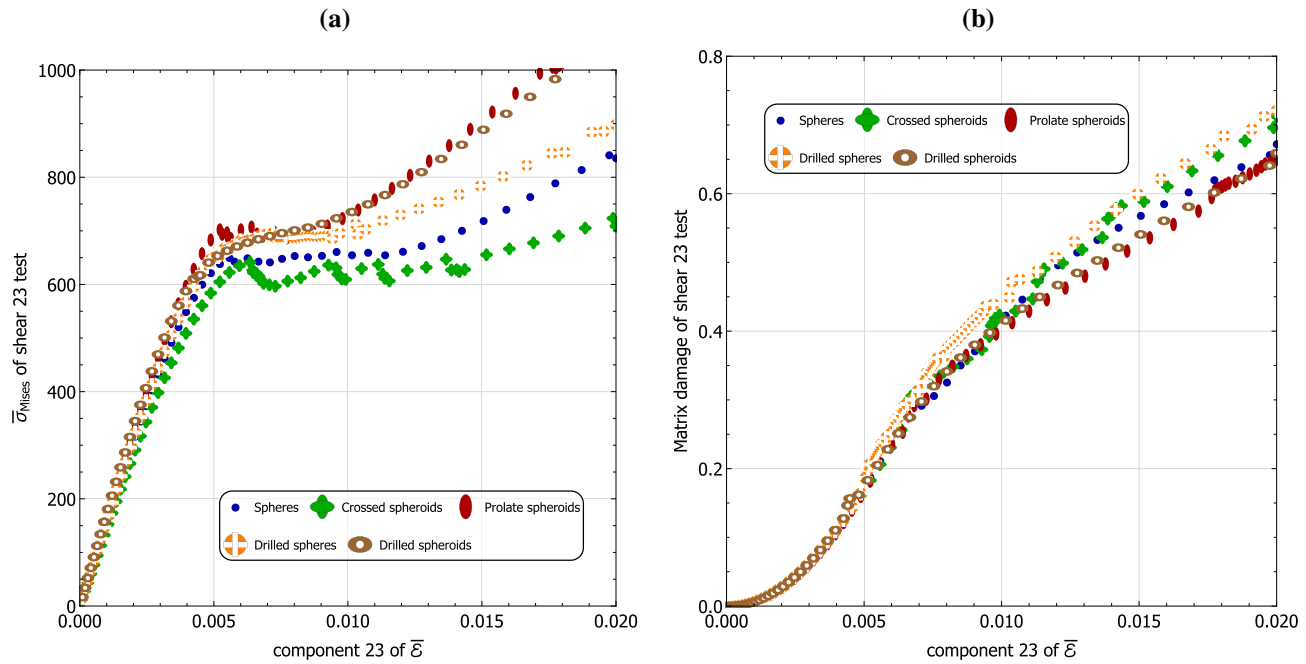

Fig. 16 MMC with the FCC particle distribution with a volume fraction $f_i = 0.3$, subjected to the shear specified by $\mathbf{E}^{(2)}$ (Eq. 19). Damage development is enabled in the matrix phase only. **a** The overall equivalent von Mises stress $\overline{\sigma}_{Mises}$, and **b** the averaged matrix damage d vs the overall strain component $\overline{\varepsilon}_{23}$

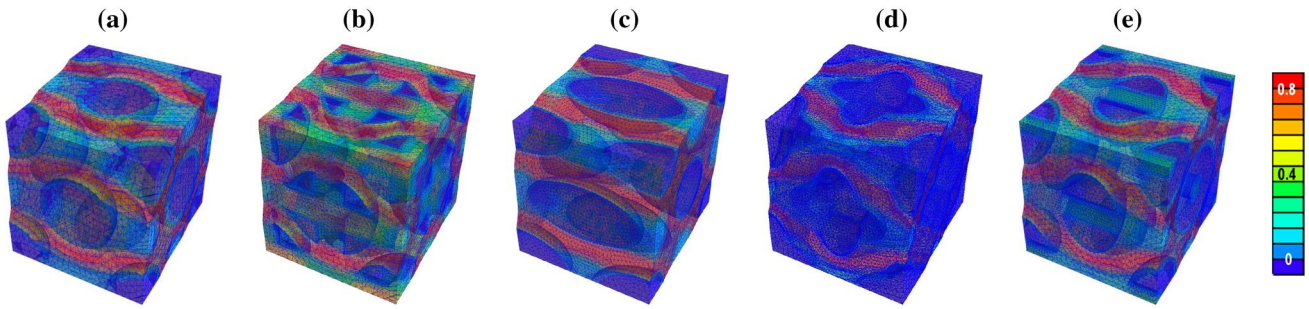

Fig. 17 Distribution of the damage parameter d (contour maps) at the strain $\overline{\varepsilon}_{23} = 0.02$ in the shear test specified by $\mathbf{E}^{(2)}$ (Eq. 19). The MMC is reinforced with ceramic particles of five different shapes: **a** spheres, **b** drilled spheres, **c** prolate spheroids, **d** crossed spheroids, and **e** drilled oblate spheroids (see Fig. 3) placed in the FCC arrangement (Fig. 9). The damage evolution law of the matrix phase is specified by Eq. C.1 (damage evolution is disabled in the inclusions)

Funding Information The research was partially supported by the project No. 2017/25/N/ST8/01968 of the National Science Center (NCN), Poland. The work of the second author was supported by the National Science Centre (NCN) in Poland under Grant No. 2015/19/N/ST8/03924.

Data Availability Statement The authors can confirm that all relevant data are included in the article.

Declarations

Conflict of interest The authors have no conflicts of interest to declare that are relevant to the content of this article.

Ethical approval This article does not contain any studies with human participants or animals performed by any of the authors.

Informed consent Not applicable.

References

1. Olson G. Computational design of hierarchically structured materials. Science. 1997;277:1237–42. https://doi.org/10.1126/science.277.5330.1237.
2. Matouš K, Geers MGD, Kouznetsova VG, Gillman A. A review of predictive nonlinear theories for multiscale modeling of heterogeneous materials. J Comput Phys. 2017;330:192–220. https://doi.org/10.1016/j.jcp.2016.10.070.
3. Clyne TW, Hull D. An introduction to composite materials. 3rd ed. Cambridge: Cambridge University Press; 2019. https://doi.org/10.1017/9781139050586.
4. Rajak DK, Pagar DD, Kumar R, Pruncu CI. Recent progress of reinforcement materials: a comprehensive overview of composite materials. J Mater Res Technol. 2019;8:6354–74. https://doi.org/10.1016/j.jmrt.2019.09.068.
5. Christensen RM. A critical evaluation for a class of micromechanics models. J Mech Phys Solids. 1990;38:379–404. https://doi.org/10.1016/0022-5096(90)90005-O.
6. Eshelby JD. The determination of the elastic field of an ellipsoidal inclusion, and related problems. Proc R Soc A-Math Phy. 1957;241:376–96. https://doi.org/10.1098/rspa.1957.0133.
7. Kanaun SK, Levin VM. Self-consistent methods for composites, vol 1: static problems. Dordrecht: Springer; 2008. p. 172–86. https://doi.org/10.1007/978-1-4020-6664-1.
8. Castañeda PP, Willis JR. The effect of spatial distribution on the effective behavior of composite materials and cracked media. J Mech Phys Solids. 1995;43:1919–51. https://doi.org/10.1016/0022-5096(95)00058-Q.
9. Torquato S. Effective stiffness tensor of composite media: II. Applications to isotropic dispersions. J Mech Phys Solids. 1998;46:1411–40. https://doi.org/10.1016/S0022-5096(97)00083-5.
10. Marcadon V, Herve E, Zaoui A. Micromechanical modeling of packing and size effects in particulate composites. Int J Solids Struct. 2007;44:8213–28. https://doi.org/10.1016/j.ijsolstr.2007.06.008.
11. Majewski M, Kursa M, Holobut P, Kowalczyk-Gajewska K. Micromechanical and numerical analysis of packing and size effects in elastic particulate composites. Compos B Eng. 2017;124:158–74. https://doi.org/10.1016/j.compositesb.2017.05.004.
12. Diani J, Gilormini P, Merckel Y, Vion-Loisel F. Micromechanical modeling of the linear viscoelasticity of carbon-black filled styrene butadiene rubbers: the role of the filler-rubber interphase. Mech Mater. 2013;59:65–72. https://doi.org/10.1016/j.mechmat.2012.12.007.
13. Majewski M, Holobut P, Kursa M, Kowalczyk-Gajewska K. Packing and size effects in elastic-plastic particulate composites: micromechanical modelling and numerical verification. Int J Eng Sci. 2020;151:103271. https://doi.org/10.1016/j.ijengsci.2020.103271.
14. Chaboche JL, Kanouté P, Roos A. On the capabilities of mean-field approaches for the description of plasticity in metal matrix composites. Int J Plast. 2005;21:1409–34. https://doi.org/10.1016/j.ijplas.2004.07.001.
15. Sevostianov I, Mogilevskaya SG, Kushch VI. Maxwell's methodology of estimating effective properties: alive and well. Int J Eng Sci. 2019;140:35–88. https://doi.org/10.1016/j.ijengsci.2019.05.001.
16. Kowalczyk-Gajewska K, Majewski M, Mercier S, Molinari A. Mean field interaction model accounting for the spatial distribution of inclusions in elasticviscoplastic composites. Int J Solids Struct. 2021;224:111040. https://doi.org/10.1016/j.ijsolstr.2021.111040.
17. Segurado J, Llorca J. Computational micromechanics of composites: the effect of particle spatial distribution. Mech Mater. 2006;38:873–83. https://doi.org/10.1016/j.mechmat.2005.06.026.
18. Dastgerdi JN, Anbarlooie B, Miettinen A, Hosseini-Toudeshky H, Remes H. Effects of particle clustering on the plastic deformation and damage initiation of particulate reinforced composite utilizing X-ray CT data and finite element modeling. Compos B Eng. 2018;153:57–69. https://doi.org/10.1016/j.compositesb.2018.07.027.
19. Escoda J, Willot F, Jeulin D, Sanahuja J, Toulemonde C. Influence of the multiscale distribution of particles on elastic properties of concrete. Int J Eng Sci. 2016;98:60–71. https://doi.org/10.1016/j.ijengsci.2015.07.010.
20. de Francqueville F, Gilormini P, Diani J, Vandenbroucke A. Comparison of the finite strain macroscopic behavior and local damage of a soft matrix highly reinforced by spherical or polyhedral particles. Eur J Mech A Solids. 2020;84:104070. https://doi.org/10.1016/j.euromechsol.2020.104070.
21. Liu LP. Solutions to the Eshelby conjectures. Proc R Soc A-Math Phys. 2008;464:573–94. https://doi.org/10.1098/rspa.2007.0219.
22. Klusemann B, Böhm HJ, Svendsen B. Homogenization methods for multi-phase elastic composites with non-elliptical reinforcements: comparisons and benchmarks. Eur J Mech A Solids. 2012;34:21–37. https://doi.org/10.1016/j.euromechsol.2011.12.002.
23. Zheng QS, Du DX. An explicit and universally applicable estimate for the effective properties of multiphase composites which accounts for inclusion distribution. J Mech Phys Solids. 2001;49:2765–88. https://doi.org/10.1016/S0022-5096(01)00078-3.
24. Du DX, Zheng QS. A further exploration of the interaction direct derivative (IDD) estimate for the effective properties of multiphase composites taking into account inclusion distribution. Acta Mech. 2002;157:61–80. https://doi.org/10.1007/BF01182155.
25. Nogales S, Böhm HJ. Modeling of the thermal conductivity and thermomechanical behavior of diamond reinforced composites. Int J Eng Sci. 2008;46:606–19. https://doi.org/10.1016/j.ijengsci.2008.01.011.
26. Kachanov M, Tsukrov I, Shafiro B. Effective moduli of solids with cavities of various shapes. Appl Mech Rev. 1994;47:151–74. https://doi.org/10.1115/1.3122810.
27. Segurado J, Llorca J. A numerical approximation to the elastic properties of sphere-reinforced composites. J Mech Phys Solids. 2002;50:2107–21. https://doi.org/10.1016/S0022-5096(02)00021-2.
28. Hassani B, Hinton E. A review of homogenization and topology optimization I—homogenization theory for media with periodic structure. Comput Struct. 1998;69:707–17. https://doi.org/10.1016/S0045-7949(98)00131-X.
29. Ranganathan SI, Ostoja-Starzewski M. Scaling function, anisotropy and the size of RVE in elastic random polycrystals. J Mech Phys Solids. 2008;56:2773–91. https://doi.org/10.1016/j.jmps.2008.05.001.
30. Hashin Z. The elastic moduli of heterogeneous materials. J Appl Mech. 1962;29:143–50. https://doi.org/10.1115/1.3636446.
31. Herve E, Zaoui A. n-Layered inclusion-based micromechanical modelling. Int J Eng Sci. 1993;31:1–10. https://doi.org/10.1016/0020-7225(93)90059-4.
32. Hori M, Nemat-Nasser S. Double-inclusion model and overall moduli of multi-phase composites. Mech Mater. 1993;14:189–206. https://doi.org/10.1016/0167-6636(93)90066-Z.

33. Suquet P. Effective properties of nonlinear composites. In: Suquet P, editor. Continuum micromechanics. Vienna: Springer; 1997. p. 197–264. https://doi.org/10.1007/978-3-7091-2662-2.
34. Mori T, Tanaka K. Average stress in matrix and average elastic energy of materials with misfitting inclusions. Acta Metall. 1973;21:571–4. https://doi.org/10.1016/0001-6160(73)90064-3.
35. Schöberl J. NETGEN—an advancing front 2D/3D-mesh generator based on abstract rules. Comput Vis Sci. 1997;1:41–52. https://doi.org/10.1007/s007910050004.
36. Korelc J. Multi-language and multi-environment generation of nonlinear finite element codes. Eng Comput. 2002;18:312–27. https://doi.org/10.1007/s003660200028.
37. Markov A, Trofimov A, Sevostianov I. A unified methodology for calculation of compliance and stiffness contribution tensors of inhomogeneities of arbitrary 2D and 3D shapes embedded in isotropic matrix - open access software. J Mech Phys Solids. 2020;157:103390. https://doi.org/10.1016/j.ijengsci.2020.103390.
38. Kowalczyk-Gajewska K, Ostrowska-Maciejewska J. Review on spectral decomposition of Hooke's tensor for all symmetry groups of linear elastic material. Eng Trans. 2009; 57:145–183. https://et.ippt.gov.pl/index.php/et/article/view/172.
39. Šmilauer V et al. Yade Documentation. 3rd ed. The Yade Project. Zenodo; 2021. https://doi.org/10.5281/zenodo.5705394.
40. Mazzucco G, Pomaro B, Salomoni VA, Majorana CE. Numerical modelling of ellipsoidal inclusions. Constr Build Mater. 2018;167:317–24. https://doi.org/10.1016/j.conbuildmat.2018.01.160.
41. Kursa M, Kowalczyk-Gajewska K, Petryk H. Multi-objective optimization of thermo-mechanical properties of metal-ceramic composites. Compos B Eng. 2014;60:586–96. https://doi.org/10.1016/j.compositesb.2014.01.009.
42. Hill R. Continuum micro-mechanics of elastoplastic polycrystals. J Mech Phys Solids. 1965;13:89–101. https://doi.org/10.1016/0022-5096(65)90023-2.
43. Kowalczyk-Gajewska K, Maździarz M. Elastic properties of nanocrystalline materials of hexagonal symmetry: the core-shell model and atomistic estimates. Int J Eng Sci. 2020;157:103393. https://doi.org/10.1016/j.ijengsci.2020.103393.
44. Celentano DJ, Chaboche JL. Experimental and numerical characterization of damage evolution in steels. Int J Plast. 2007;23:1739–62. https://doi.org/10.1016/j.ijplas.2007.03.008.
45. Steinmann P. Formulation and computation of geometrically nonlinear gradient damage. Int J Numer Methods Eng. 1999;46:757–79. https://doi.org/10.1002/(SICI)1097-0207(19991020)46:5757::AID-NME7313.0.CO;2-NN.
46. Rutecka A, Kursa M, Pietrzak K, Kowalczyk-Gajewska K, Makowska K, Wyszkowski M. Damage evolution in AA2124/SiC metal matrix composites under tension with consecutive unloadings. Arch Civ Mech. 2020;20:135. https://doi.org/10.1007/s43452-020-00134-x.